Nano Energy 87 (2021) 106224

Contents lists available at ScienceDirect

Nano Energy

journal homepage: www.elsevier.com/locate/nanoen

Full paper

Moisture-participating MOF thermal battery for heat reallocation between indoor environment and building-integrated photovoltaics

Effrosyni Gkaniatsou [a,1], Bin Meng [b,1], Frédéric Cui [b,c,*], Roel Loonen [b], Farid Nouar [a], Christian Serre [a,**], Jan Hensen [b,**]

[a] Institut des Matériaux Poreux de Paris (IMAP), UMR 8004 CNRS, ESPCI Paris, Ecole Normale Supérieure de Paris, PSL University, 75005 Paris, France
[b] Department of the Built Environment, Eindhoven University of Technology, P.O. Box 513, 5600 MB Eindhoven, the Netherlands
[c] Department of Civil Engineering, Technical University of Denmark, Brovej Building 118, DK-2800 Kgs. Lyngby, Denmark

ARTICLE INFO

Keywords:
Thermal energy
Sorption
BIPV
Metal-organic frameworks
Nano-porous
Built
Environment

ABSTRACT

The present deployment of photovoltaic (PV) panels on the rooftop has been far below its potential. Stakeholders often see the PV as a strong design constraint, isolated from the built environment and not adapted to their requirements. Here, we propose a new design that combines the PV panels with a metal-organic framework based sorptive thermal battery, which serves as a multi-functional building element and is more actively involved in the indoor environment regulation. The open-loop thermal battery can stock moisture from air with 10^5 times its volume so that the built environment with high humidity at night is dried to a comfortable and healthy level. The moisture is removed at daytime with unpleasant solar heat, thereby cools the PV panels simultaneously, improving electricity generation by 5%. The benefits of this design can be translated into economic added value to facilitate investment decisions of building-integrated PV projects.

1. Introduction

The European Commission pledged to reduce emissions by more than 50% by 2030 in the EU's climate target [1], which requires a more rapid move from fossil resources to renewable energy consumption. Photovoltaic (PV) installation has reached 130 TWh in 2019 in Europe, which represented 4.8% of the final electricity demand and shared 42% of the yearly increased power generation capacity. With the electricity generation costs fall below to $2ct in many regions over the world, Photovoltaics will play an essential part to mitigate climate change in next decades [2,3]. Though a centralized PV plant is an effective way to benefit from scaling-up, an apparent disadvantage in the current situation is its high cost related to delivering electricity to appropriate places at the appropriate time [4]. Building integrated photovoltaic (BIPV) is an intuitive answer to this challenge. By directly integrating into façades and rooftops to exploit the incident solar radiation to the building envelopes, BIPV can avoid most investment and operational fees on transmission [5]. So far, the system represents roughly half of Europe's cumulative solar panel installation [4]. However, its total share in final energy consumption falls much below the actual technological potential estimated from various aspects [6], and the growth is often slowed down at buildings' design or construction stage due to the limited choice in its functionality and strong technical constraints [7]. On one hand, the academic research and energy industry consider BIPV, to a great extent, as a mere sub-branch of the PV sector, emphasizing the levelized-cost of electricity and the adaptation to building skins in different shapes [8,9]. On the other hand, architects and builders only perceive the solar panels as a solid, semi-transparent raw material or add-on containing restricted esthetic features, which provide basic shelter functions such as weather protection and thermal insulation. The BIPV must offer more possibilities as a multifunctional built element that can be recognized by actors along the value chain to accelerate its market penetration.

In this study, we propose a new design that combines a sorptive thermal battery based on metal organic-frameworks (MOFs) and the BIPV, which leads to a deeper interaction between the PV and the building. This system alternately harnesses the waste heat from the built environment and BIPV to fine-tune occupants' comfort (Fig. 1). In calm weather, the moisture content in the air remains somewhat steady, but

* Corresponding author at: Department of the Built Environment, Eindhoven University of Technology, P.O. Box 513, 5600 MB Eindhoven, the Netherlands.
** Corresponding authors.
E-mail addresses: f.s.cui@tue.nl (F. Cui), christian.serre@espci.fr (C. Serre), j.hensen@tue.nl (J. Hensen).
[1] These authors contributed equally to this work.

https://doi.org/10.1016/j.nanoen.2021.106224
Received 25 March 2021; Received in revised form 18 May 2021; Accepted 1 June 2021
Available online 12 June 2021

the relative humidity (RH) fluctuates along with the diurnal/nocturnal temperature swing (Fig. 2a). A high level of humidity can cause deterioration of building materials and biological growth and, therefore, has a significant effect on building structural capacity, envelope appearance, and occupants' health [10]. Fig. 1 shows the main idea of the BIPV-thermal battery system. During the night, the highly humid air from an indoor environment or adjacent zones is naturally or mechanically ventilated to the PV thermal battery and dried. This discharging process enables the thermal battery to harvest the low-grade latent energy from the moisture instead of removing it with electricity input. The thermal battery will be charged later during the daytime, absorbing heat from the solar panel and releasing water vapor in an endothermic desorption process. The moist and warm air will then be evacuated to the ambiance or interior space. Owing to the large amount of water left from the thermal battery, the PV panels can operate at a lower temperature.

Unlike traditional thermal batteries based on liquids, molten salts, or paraffin phase-change materials (PCM) that absorb energy from heat sources or deliver energy to heat sinks with temperature differences, sorptive thermal batteries based on nano-porous materials work in cycles driven by adsorption potential difference to the moisture (water vapor pressure). MOFs are an emerging class of advanced hybrid micro- or meso-porous water adsorbents with large pore volumes and a tunable hydrophilic/hydrophobic balance, that show many advantages for their use in sorptive thermal batteries [11,12]: (i) Low regeneration temperatures with high enough cyclic water uptakes, situated in PV's working conditions. (ii) Solid-state and facile shaping methods that allow easy coating or packing to the PV rear side or joint surfaces for heat exchange. (iii) The adsorption of water occurs via reversible and continuous pore filling on the internal surface of pore structure [13], which avoids problems of leakage and corrosion, typically appearing among existing absorbents, e.g., hygroscopic salts in liquid or encapsulated forms. (iv) Long-term hydrothermal stability [14,15] that fits for a 20–30 years lifetime, coherent with newly or already deployed PV systems. (iv) Large-scale, low-cost production is possible [16,17].

Recent research advances on sorptive thermal batteries have investigated heating or cooling buildings, electronics, PV, thermoelectric devices, lithium batteries [18–23], etc. These systems were

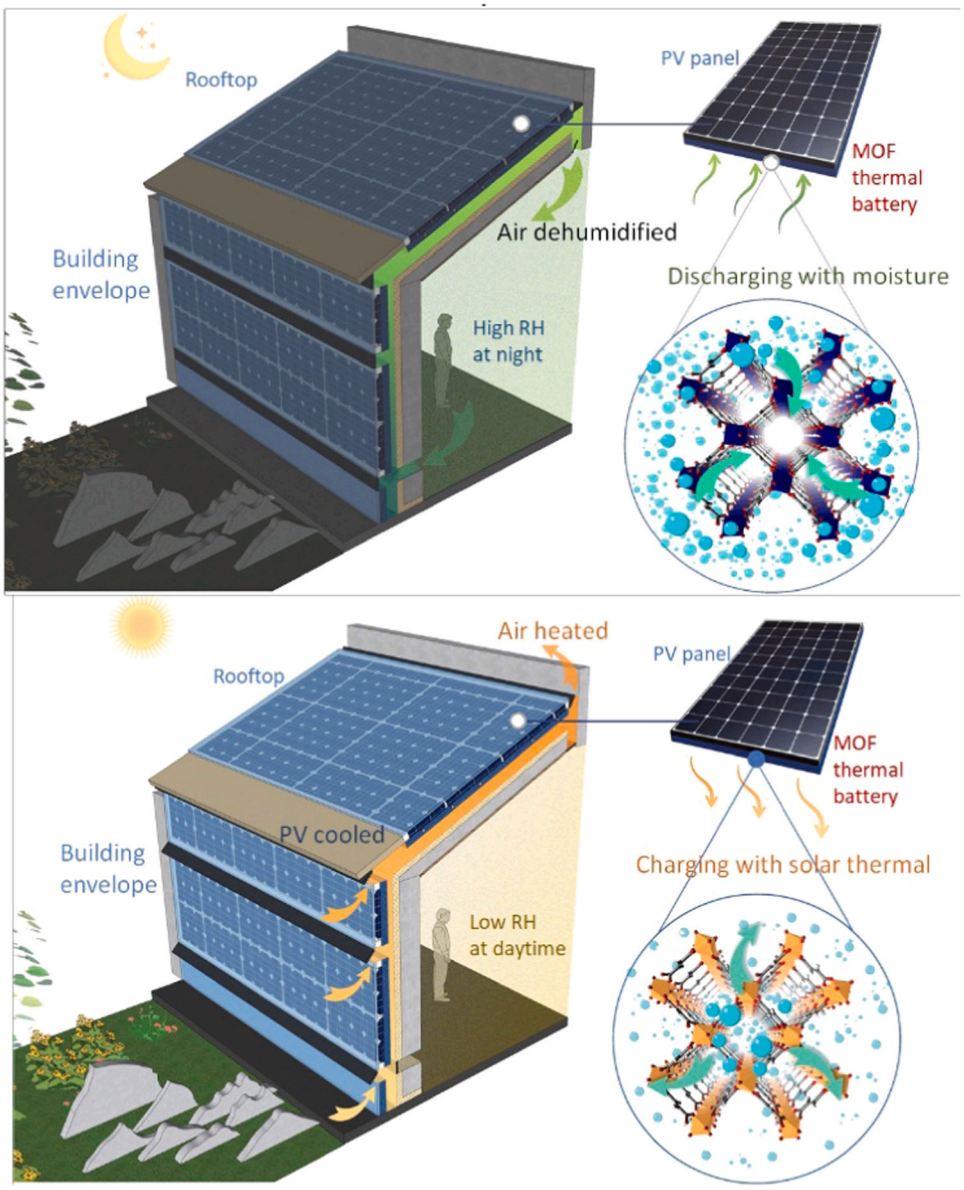

Fig. 1. Working principle of the MOF thermal battery combined with BIPV. Schematic illustration of the interaction between PV thermal battery and the built environment. The thermal battery is discharged with moisture at night and charged by absorbing solar thermal energy, which cools the PV panel.

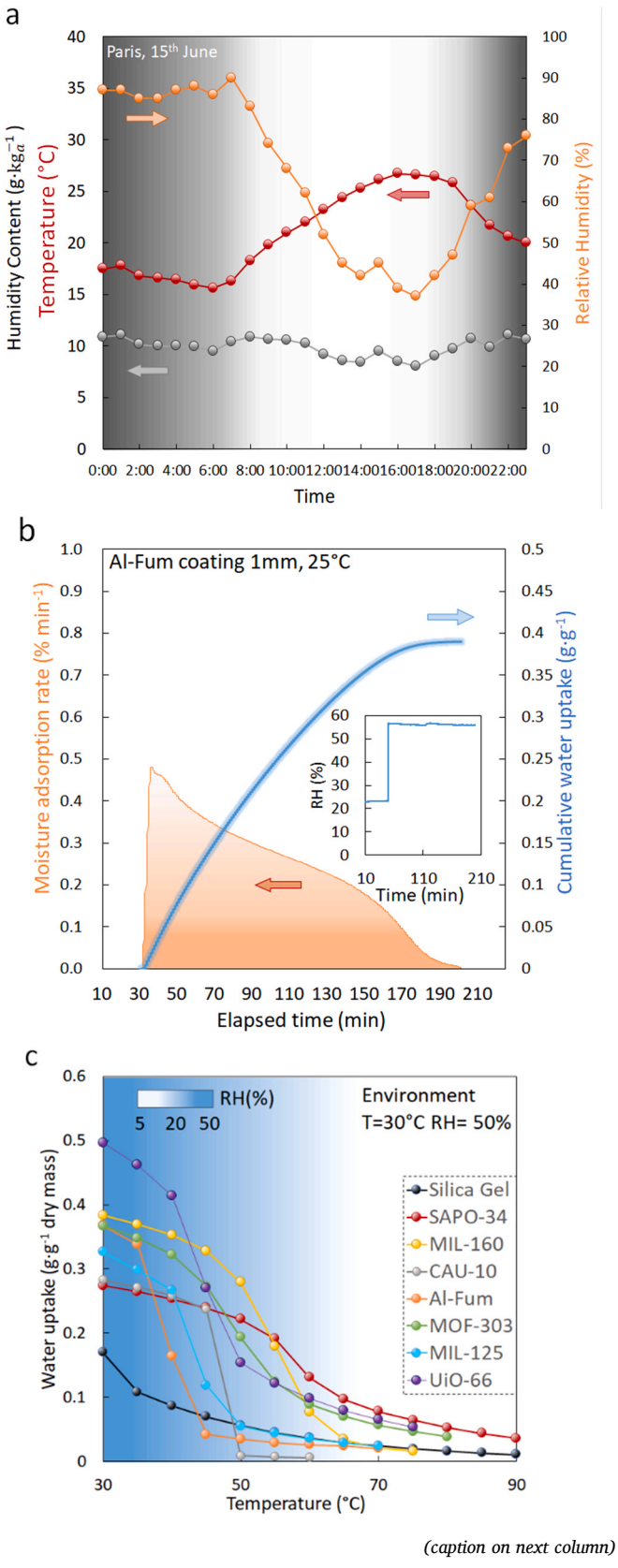

(caption on next column)

Fig. 2. Feasibility in bi-directional heat reallocation of the thermal battery (a) Weather data of a typical sunny day in Paris' summer. The absolute humidity remains steady while the relative humidity is fluctuating. The thermal battery dries the indoor environment at night and releases vapor at daytime. (b) Instant moisture adsorption rate and cumulative water uptake of an open-loop sorptive thermal battery based on MOF Aluminum-Fumarate from a hygro-gravimetric test. Shaded zones represent the measurement uncertainty. The inset is the applied humidity level. (c) Isobaric heating of thermal batteries constructed with typical MOFs, zeolite and silica gel under a summer day condition. The background color map represents the estimated RH on the interfacial layer between the sorbents and the environment. Owing to the large amount of water desorbed in a narrow relative pressure change, the MOFs will form a temperature plateau when exposed to stable heat flux. (For interpretation of the references to color in this figure legend, the reader is referred to the web version of this article.)

characterized by high compactness compared to PCM thermal batteries [24]. However, they couldn't differentiate from the latter in the cooling function and cost model, by taking into account the surrounding environment solely as a heat sink. Here, we show theoretically and experimentally the MOF thermal battery system can dry the air up to 10^5 times of its volume by 15%RH, covering the dehumidification needs of the indoor environment, which served as a latent heat source. The thermal battery gains an equivalent cooling effect on the PV panels attached to the same indoor space, increasing the solar-electricity conversion by 4–5% in an outdoor test. The benefits have a concurrent effect on producing and consuming energy, as well as improving the built environment and prolonging buildings' lifetime.

Our concept illustrates a more active working mode of the PV thermal battery in bi-directional heat reallocation, with both ends of the thermal battery mutually being resources and objectives. The multifunctional behavior can balance the additional cost for the implementation of such an innovative system in the effort to improve the levelized cost of electricity (LCOE), and also inspire a more holistic economic analysis pattern in addition to the LCOE [25,26]. The aim is to engage more stakeholders in BIPV projects. After all, BIPV is not only about an energy supply attachment but also the deep involvement in building engineering.

2. Conception of PV-thermal batteries with MOFs

A sorptive thermal battery is an open-looped sorption heat pump that reversibly captures and releases water vapor and, at the same time, exchanges enthalpy with the environment. The performance optimization depends on several metrics in common with other water sorption applications, such as massive water uptake, S-shaped isotherms with no hysteresis, fast kinetics, etc.

Based on these criteria, we chose several suitable MOFs and deposited them to the PV rear side to fabricate sorptive thermal batteries. For instance, MIL-53(Al)-Fum (MIL = Materials from Institut Lavoisier) or Aluminum Fumarate (Al-Fum), is a benchmark MOF for water sorption application. It has a three-dimensional framework, composed by 1D chains of corner-sharing Al(III) octahedra, connected together by fumarate ligands, with a relatively high surface area (1100 m^2 g^{-1}) [27]. Al-Fum has been commercialized by BASF under the name Basolite A520 [28], is composed by low-cost and non-toxic reactants, can be produced at a large scale and shows a good water stability. All these, makes it an ideal candidate for the open-loop thermal battery.

Sorption properties are essential in the discharging process. Fig. 2b shows the sorption curve of a 1 mm-thick sample of MOF Al-Fum, under constant relative humidity and a flow speed of 0.8 m s^{-1}, which can be easily obtained in air ducts or channels with buoyancy or wind effects [29]. When the humidity is at a higher level than the main sorption step, the final mass augmentation is about 40% of the dry material, corresponding to a heat storage capacity of 0.88 MJ kg^{-1} dry mass, quadruple to most PCMs. The instant sorption rate curve indicates the

average specific power of 125 W kg^{-1} to remove the latent energy load in the 90% adsorption (discharging) range ($\tau_{90\%}$).

The thermal batteries with hydrated MOFs are charged by the heat dissipated from PV. Fig. 2c exhibited the desorption behavior under a representative summer condition (30 °C, 50%RH) for several benchmark adsorbents. In contrast to silica gel, MOFs with S-shaped isotherms manifest a water uptake drop in a narrow temperature range. Most of these MOFs are less hydrophilic than the zeolite SAPO-34, and the desorption happens at a temperature lift from 15 °C to 45 °C, covering most of the PV's working temperature during the daytime.

3. Heat reallocation performance of small-scale PV-thermal

We use three Al(III) dicarboxylates MOF materials including Al-Fum [30], CAU-10 (CAU = Christian-Albrechts-Universität) [31] and MIL-160 [32], in a lab test to validate the thermodynamic feasibility of heat reallocation. These MOFs are microporous water sorbents with different hydrophilic character, from very hydrophilic (MIL-160), moderate hydrophilic (CAU-10) to weakly hydrophilic (Al-Fum), as deduced from their water sorption profiles (Table 1), which can further reveal the criteria of working materials for a sorptive thermal battery. The synthesis of these MOFs has been systematically carried out under green and scalable conditions following reported procedures; details about the production methods and characterization of the materials can refer to the Supplementary Note 1.

Small PV thermal battery modules were fabricated based on solar cells (18 V-5 W, 567 cm^2) coated with 10 g of sorbents. The sorbent layers were around 0.7 mm thick with the porosity varying from 0.5 to 0.65 ($\varepsilon = 1\text{-}\rho_{sorbent}/\rho_{MOF}$) (Fig. 3a, b). For comparison, another thermal battery using silica gel was tested following the same protocol. The modules were at first placed under the condition of 25 °C, ~90%RH to achieve equilibrium on a highly hydrated state, and then moved into an air-conditioning room interfaced with a solar simulator. The solar module was attached to a large plate (2 m^2) to minimize the convection effect from the ventilation system on the rear side, and the plate was installed at a small distance (10 cm) to the glass shield of the solar simulator, which created a laminar flow over the PV surface (Fig. 3c). A solar flux of 1 sun (1 kW m^{-2}) was introduced to the PV thermal battery and the room was maintained at 25 °C, ~40%RH.

The evolution of PV's rear side temperature and the current-voltage characteristics are shown in Fig. 3d, e. The slope of temperature decreased gradually until achieving the balance between solar-to-heat and convection cooling effect at 63 °C. Adding thermal batteries based-on MIL-160, CAU-10, Al-Fum, Silica Gel slowed up the process by 880 s, 580 s, 680 s, and 120 s, respectively. The sorbents with apparent sorption steps would induce a temperature plateau where the majority of water uptake was released. This temporary cooling effect led to higher electricity generation, since this PV's temperature increase at each degree would result in a 0.4% loss in conversion efficiency (Fig. S8). Owing to the thermal batteries, PV panels produced 1.2% (silica gel), 3.0% (MIL-160), 4.0% (CAU-10) and 5.1% (Al-Fum more electricity in total than the original one. Because of the ability to take cooling effects quicker at lower temperatures, the less hydrophilic sorbents such as Al-Fum offered a broader working range. Yet, a sorption step less than RH50% is appreciated to guarantee the thermal battery's function in most climates and to ensure that charging occurs at 20 °C higher than the ambient temperature, a situation that is usually accompanied by more intensive solar irradiance.

Fig. 3f gives the derived cooling power and enthalpy removed by the Al-Fum thermal battery during the solar-driven charging. During the first stage of temperature ramping, the evacuated heat increased very slowly as the surrounding relative humidity remains higher than the main sorption step. After 500 s, the cooling power soared while reaching the temperature plateau. The peak cooling power reached more than 450 W m^{-2} at this condition. Certainly, the thicker the layer in achieving longer working time, the lower the average specific cooling power as a result of hindered vapor movement within the sorbent. Fig. 3g presents the gravimetric and volumetric energy density of the tested thermal batteries, both 4–5 times above the commercialized non-porous paraffin PCM storage system, which reveals the high compactness of sorptive technology. Compressing or packing the MOFs at a lower porosity can have an even higher volumetric energy density, offering a light-weight solution in building envelope scenario but may also bring down the heat and mass transfer performance [33,34].

4. Theoretical prediction of the PV thermal battery performance

While most demonstrations on sorption thermal battery under laboratory conditions benefited from the high energy density of advanced sorbents and achieved superior performances for heat reallocation at small-scale, the fundamental limits linked to sorbents' properties appeared in scaled-up engineering design and the corresponding optimization strategies in practice have not been investigated. Many possible routes for identifying problems and optimizing the design can find inspiration from current technologies. For instance, removing or utilizing undesired residual heat from PV has been a long pursuit in recent research efforts. Eventually, the dissipated or collected heat will be stored in a thermal battery [35,36] and the most common in-situ thermal batteries are PCM-based PV cooling systems, with reported field tests providing 1–5% enhancement in the electricity generation [37–39]. Despite attempts in early stage to localize the thermal effect of PCMs [40], so far the existing products use PCMs in their bulk form. The more PCMs deployed, the more challenges appear in affiliated investment, flexibility, space constraints, esthetics, etc., whose consequences are often absent in cost analyses, but are essential for the market penetration. Such troubles in thermal insulation to prevent stationary

Table 1
Main properties of tested adsorbents for the application of open-loop thermal battery.

Material	Formula	Crystal density (g cm^{-3})	Pore volume (cm^3 g^{-1})	BET surface (m^2 g^{-1})	Water uptake (g g^{-1})[a]				Enthalpy absorbing capacity (Wh kg^{-1})[b]			
					Relative humidity (%)				Temperature lift (°C)			
					15	25	40	90	20	30	40	50
MIL-160	Al(OH)($C_6H_2O_5$)	1.07	0.398	1070	0.307	0.353	0.374	0.407	54	101	241	307
CAU-10	Al(OH)($C_8H_4O_4$)	1.15	0.285	660	0.001	0.255	0.273	0.312	39	164	245	250
Al-Fum	Al(OH)($C_4H_2O_4$)	1.06	0.489	1100	0.033	0.053	0.343	0.422	178	307	317	318
Silica gel	SiO_2	1.35	0.44	760	0.048	0.076	0.113	0.305	157	181	197	209

[a] Water uptake at 25 °C. The change in function of RH is limited at different temperature (Fig. S4).

[b] Deduced from the isosteric enthalpy of water adsorption (Fig. S5). Materials are initially hydrated at 90%RH, 25 °C.

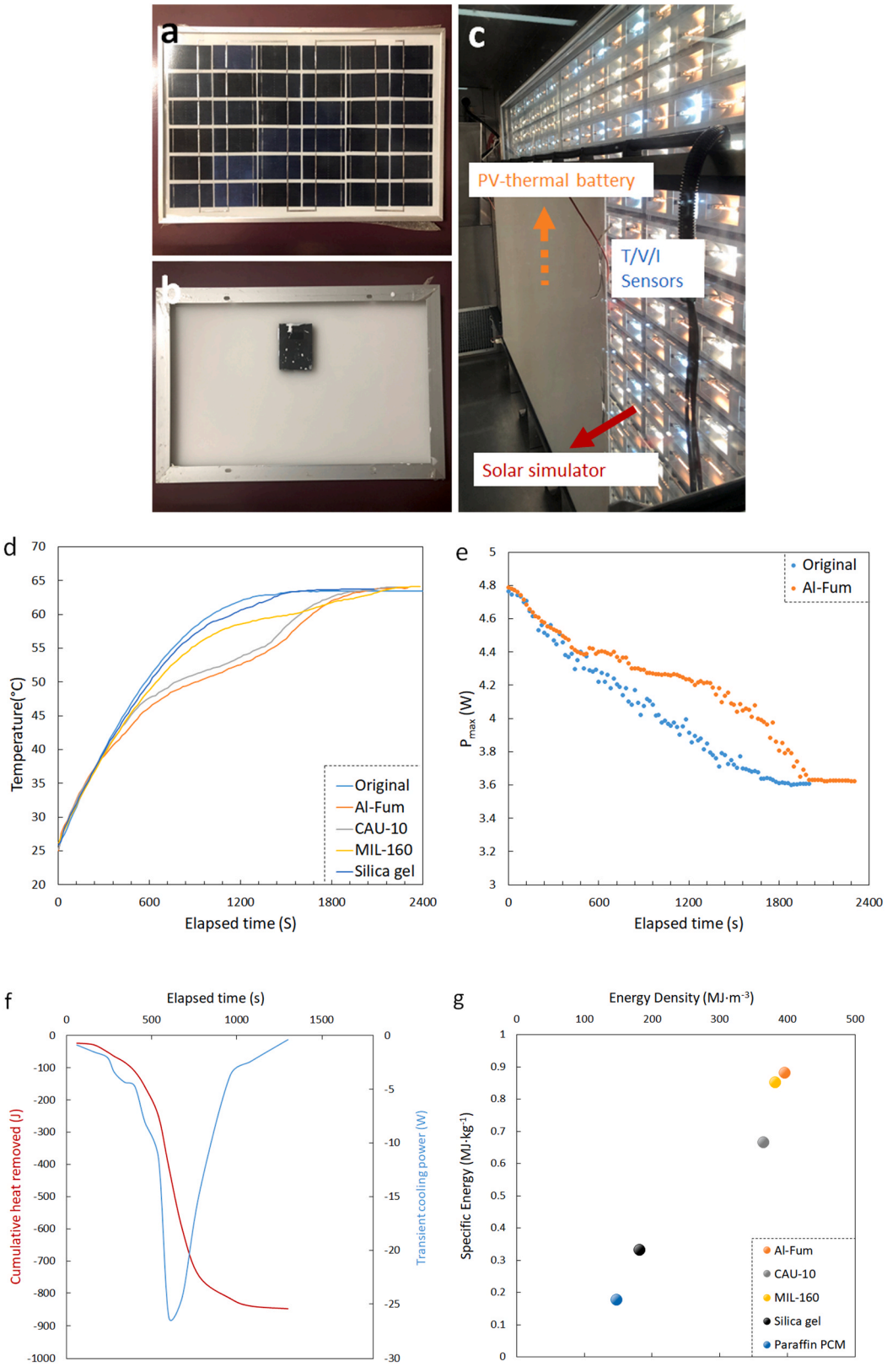

Fig. 3. Laboratory characterization of thermal batteries' thermodynamic limitation. All tests performed under 1000 W m^{-2}, ~40%RH at 25 °C. (a,b) Photos of the PV thermal battery: front side and rear side. (c) Photo of the lab test set-up. (d) PV's rear side temperature evolution. The 'original' sample denotes PV with no sorbent. (e) Electricity power output of the PV. (f) Experimentally-derived transient cooling power and cumulative heat removed by the thermal battery during the charging process. The results in (e,f) were plotted only with Al-Fum for clarity. Values for other materials can be found in Fig. S7. (g) Comparison of the energy density of various thermal batteries including sorptive thermal battery with MOFs and silica gel, as well as the commercial paraffin-PCM.

losses to the environment and in bulky components are exempted for a sorption cycle. The high energy density of the sorption cycles can promote the implementation suitable for more application scenarios. However, a fundamental issue similar to PCMs also exists for sorption thermal batteries and should not be neglected. That is, a thicker layer of MOF in an up-scale application can have an adverse effect on the cooling effect.

Metrics to bridge the demonstration at the level of material science and proper engineering designs need further clarification. To tackle this challenge, we developed a numerical model to evaluate and optimize the performance of the PV thermal battery with coupling heat and mass transfer models in MATLAB and with PV performance simulations using PV-lib (Supplementary Note 2). In Fig. 4a, we mapped the working principle of the MOF Al-Fum thermal battery to the test conditions. The open-loop sorptive thermal battery undergoes the locus through the isosteres curves of Al-Fum, constructed from isotherms at different temperature. Usable energy density was directly determined by the cyclic water uptake between discharged (blue point) and charged (red point) states. Discharging or charging of the thermal battery can be simply triggered or deactivated by the contact to/isolation from environment with mechanical doors/valves to control the working time (green point). In confined space, air was dried to a lower humidity level at night, which approached the inflection point of Al-Fum's isotherm. A slight temperature increase can be observed in reality due to the exothermic reaction. Air was humidified at daytime by receiving the vapor from the thermal battery, but the RH decreased (Fig. S9). The airflow is evacuated to the ambient environment in summer, and can be conveyed to indoor environment as a preheating process in winter.

The temperature of the original PV panel is a balance mainly between the solar irradiance input and the cooling effects from convection and radiative cooling (Fig. S10). Our model considered the additional cooling capacity and thermal resistance of the charging process brought to the system. We carried out a sensitivity study on the sorbent layer thickness (1, 5, 7 mm) to find out the appropriate configuration of the sorbents in practice (Fig. 4b).

The kinetics of the system is a figure-of-merit as important as the thermodynamic properties but is often neglected in analyses [41,42], however, the transfer kinetics can be sometimes more critical than the

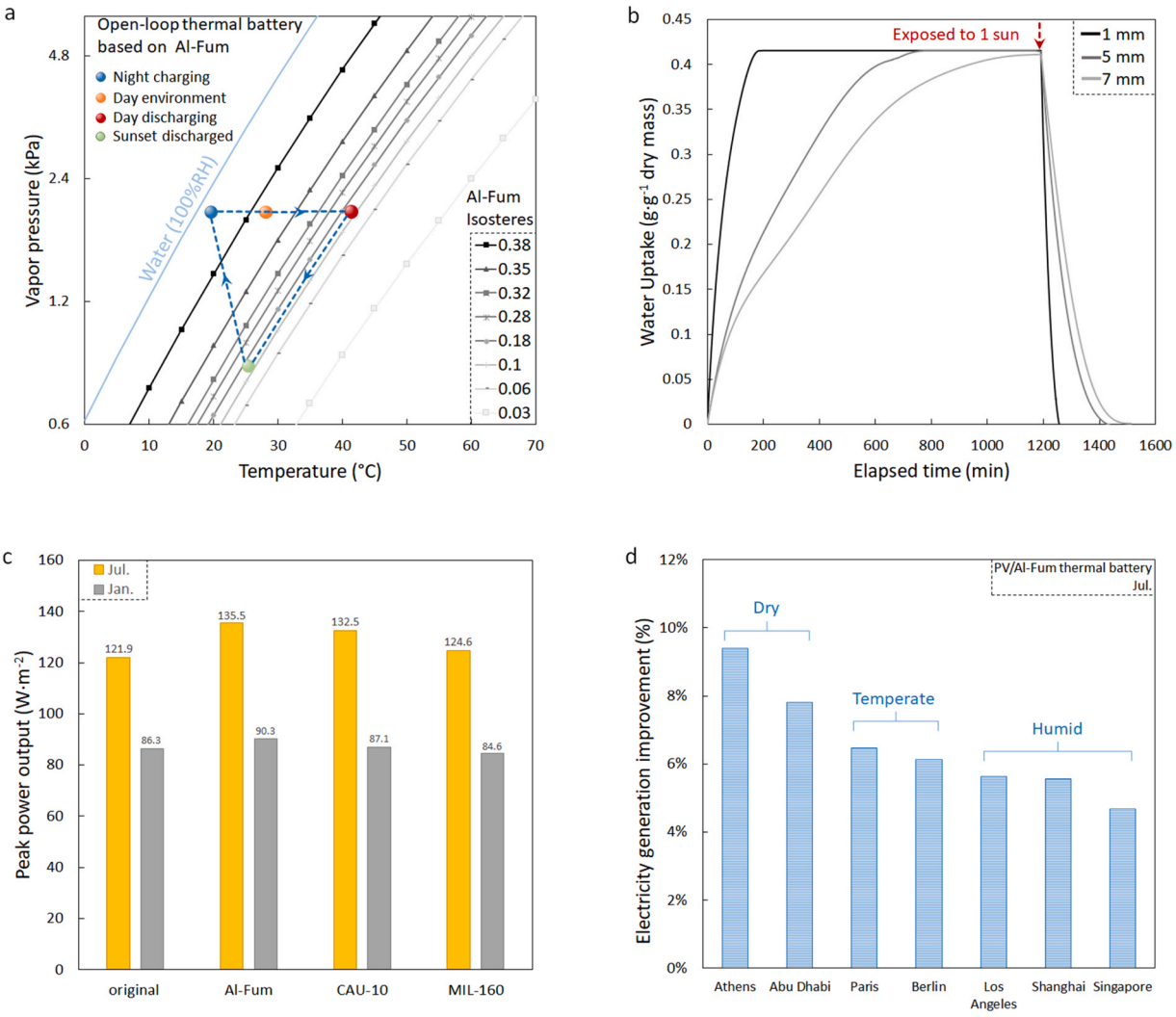

Fig. 4. Integrated PV thermal battery's performance in built environment. (a) Isosteric cycle diagram of an open-loop sorptive thermal battery. The saturated water vapor is represented by the blue line and sorption equilibriums (Isosteres) of Al-Fum are represented by lines with different gray scales. The thermal battery was initially hydrated at night (90% RH at 20 °C). The temperature increased at daytime with sun exposure, desorbing water vapor. After charged, the thermal battery can be isolated from the environment to be kept in dry state until dehumidification is necessary, otherwise it can freely adsorb vapor from air, following the reverted locus from the red point to the blue point. (b) Predicted sorption cycles of various coating layers under 1 sun illumination. Thermal batteries with three layers of 1, 5 and 7 mm layers can reallocate heat of 0.39, 1.9, and 2.8 MJ m^{-2} per charging cycle, respectively. (c) Peak performance in Paris of various MOF thermal batteries in representative summer and winter days. (d) Average PV performance improvement of Al-Fum thermal battery in 7 cities in a representative summer day. (For interpretation of the references to color in this figure legend, the reader is referred to the web version of this article.)

water uptake capacity of the sorbents. While, the mass transfer is less a constraint in desorption at a higher temperature, the heat transfer is, which significantly impaired the cooling effect in charging by solar heat. The three sorbent layers had adsorption time of 125, 480 and 680 min ($\tau_{90\%}$), respectively, which were validated by the experimental data, and desorption time of 45, 155 and 185 min, respectively. In a total charging cycle, thermal batteries with three layers can reallocate heat of 0.39, 1.9, and 2.8 MJ m^{-2}, respectively.

We run the PV performance simulation for a variety of climatic conditions. Fig. 4c shows the peak electricity generation of the original PV and with the MOF thermal battery in Paris. The PV panels can produce 11.1%, 8.6% and 2.1% more electricity in summer and 4.6%, 1%, and negligible effect in winter, with the thermal batteries based on Al-Fum, CAU-10 and MIL-160, respectively (Fig. S12).

A PV MOF thermal battery is a more 'climate-adaptive' solution [43] than a PCM system (Fig. S11). The usually adopted design strategy for a PV-PCM system is to choose working materials with melting points as low as the upper bound temperature of local weather (e.g., RT30, A40 to absorb heat at 30 °C and 40 °C in summer) to attain a maximum solar thermal storage capacity. Even so, the PCMs would be unable to absorb the majority of solar heat in winter for regions given seasonal temperature variation. In contrast, the shape of sorption isotherms of MOFs remains the same at various temperatures, which means a MOF thermal battery can autonomously respond to seasonal alternations and shows little cyclic performance fluctuation (Fig. S4).

MOFs are more robust in adapting to seasonal variations, e.g. Al-Fum can still keep half of its performance in winter in such a temperate climate (charging at 45 °C in summer and 25 °C in winter, Fig. S3), which is more favorable than the working conditions of PCM thermal battery. We then calculated Al-Fum thermal battery's performance for a representative summer day in seven cities with various altitudes and climates (Fig. 4d). The tendency is perspicuous that the MOF thermal battery works more effectively at higher irradiance levels and in drier weather with cities like Athens and Abu-Dhabi being the most relevant to take benefit from the open-loop thermal batteries system.

5. Optimal design of thermal battery based on performance, practicability and scalability

The cooling performance of the charging process can be evaluated by the compounded results of three metrics: the temperature plateau deviated from the maximum temperature of the original PV panel, the effective duration created by unit mass of the working materials, and the final temperature lift due to additional thermal resistance after the thermal battery is fully charged (Fig. S20). The design strategy is clear that finding the optimal thickness to achieve intra-day operation with minimum thermal resistance.

The temperature plateau that a sorptive thermal battery creates is notably determined by the position of the sorption step on the isotherm, namely, the inflection point of an S-shape sorption curve. A less-hydrophilic sorbent can release water vapor at a lower temperature as the relative humidity of the surrounding microclimate drops below its inflection point more quickly in a temperature ramping process.

The effective cooling duration and the final temperature lift are mainly determined by the thickness of the MOF layer under given environments. The MOF layer should be thick enough to maintain a long cooling effect during the daytime but not too thick since the increased temperature lift will offset the temperature plateau. As showed in the small-scale tests and thermodynamic analysis above, a very thin layer Al-Fum thermal battery creates an effective cooling effect at 25 °C above ambient temperature while the effective time is less than half an hour. A thick layer of 16 mm will elongate the cooling duration to 6 h but can have a final temperature lift of 10 °C, and the cooling temperature plateau moves along with it. Hence, the temperature deviation to the original PV narrows down, and the cooling effect for the unit mass of adsorbent decreases (Fig. S21). This deterioration of a thick layer is acceptable for a day with strong irradiance and no wind, because the original PV temperature can reach 50 °C above ambience. However, when the irradiance is weaker, less than 600 W m^{-2} for instance, the original PV temperature decreases to 25 °C above ambience, which limits the allowable layer thickness to 8 mm. A stronger wind is favorable for a thicker layer because the improved heat transport can enable the charging at a lower temperature to approach the thermodynamic limit of the sorbents.

A very hydrophilic MOF such as MIL-160 can work in more arid weather and maintain a more intensive cooling effect per unit mass deployed under very high solar irradiance. Since very hydrophilic MOFs have a stronger affinity to water molecules, the cooling effects are generated at higher temperatures. When the irradiance is weak, the temperature of the original PV panel decreases and the thermal heat may not be sufficiently high to charge very hydrophilic MOFs. The two effects constrict the operation window of the thermal battery. A 30 °C temperature lift can charge all the Al-Fum thermal battery (inflection point at 25%RH) but only half of CAU-10′s storage capacity (inflection point at 18%). A 30 °C temperature lift is needed for MIL-160 (inflection point at 8%RH) to fully charged regardless of its similar maximum water uptake to Al-Fum. However, too weak hydrophilicity will trigger the charging of the thermal battery at low temperature and is ineffectual to improve electricity generation at too low irradiance. As a trade-off, an inflection point residing between 25% and 40%RH would be appropriate for this application in most climates. A detailed study of the optimal thickness in the function of irradiance and hydrophilicity is presented in Figs. S23 and S24. We also showed the effect of hydrophilicity on the discharging and charging performance in various weather in Figs. S25–S27.

Among the suitable materials, we chose to apply in priority Aluminum-series MOFs for the low-cost and scalability (less expensive metals and ligands, green synthesis), even if they may not always outperform other MOFs. Under realistic conditions in Paris, the kinetics would be faster than in the lab test due to the wind effect and the solar flux is much lower than 1000 W m^{-1} for most time in 1 day, therefore, we chose the sorbent layer of 7 mm for further demonstration in the field test as a trade-off.

6. Proof-of-concept of an Al-Fum thermal battery combined with BIPV

Finally, the new design was investigated under real summer conditions. Since the Al-Fum thermal battery outperformed other sorbents under laboratory conditions and in simulation for various climates, we chose Al-Fum for the outdoor test. A proof-of-concept BIPV-MOF thermal battery was built on a solar cell (8 W-697 cm^2) with Al-Fum coating (215.8 g, 7.5 mm) and associated modules including a Plexiglas box (0.5 m^3) and ventilators to simulate an indoor space (Fig. 5a). The PV-thermal battery was inlaid in the upper side of the Plexiglas box with the Al-Fum layer facing the interior space. The thermal battery was dried and sealed up until the test, starting from the evening. The night discharging by ambient moisture was initiated and maintained by setting the flow at 0.8 m s^{-1}, yielding an air change rate around 7.2 vol h^{-1}. The PV was covered until the second day of charging process powered by natural sunlight. A blank PV sample was placed aside also on a fanned box for comparison. Temperature profiles of both blank PV and PV thermal battery captured with an infra camera show an apparent distinction even for the front sides (Fig. S14).

The hygrothermal measurements at the inlet and outlet of the interior space marked an average dehumidification effect of 1.6 g kg^{-1} (around 15%RH) during 12 h (Fig. 5b). The thermal battery was 0.52 L in size, so the dried air reached up to 83,000 times of its volume when the water uptake capacity diminished by the end of discharging. A fast humidity ramping-up could be observed as soon as the solar flux was above 600 W m^{-2}, which triggered desorption. Air temperature underwent a rapid increase then stabilized at a plateau for a few hours,

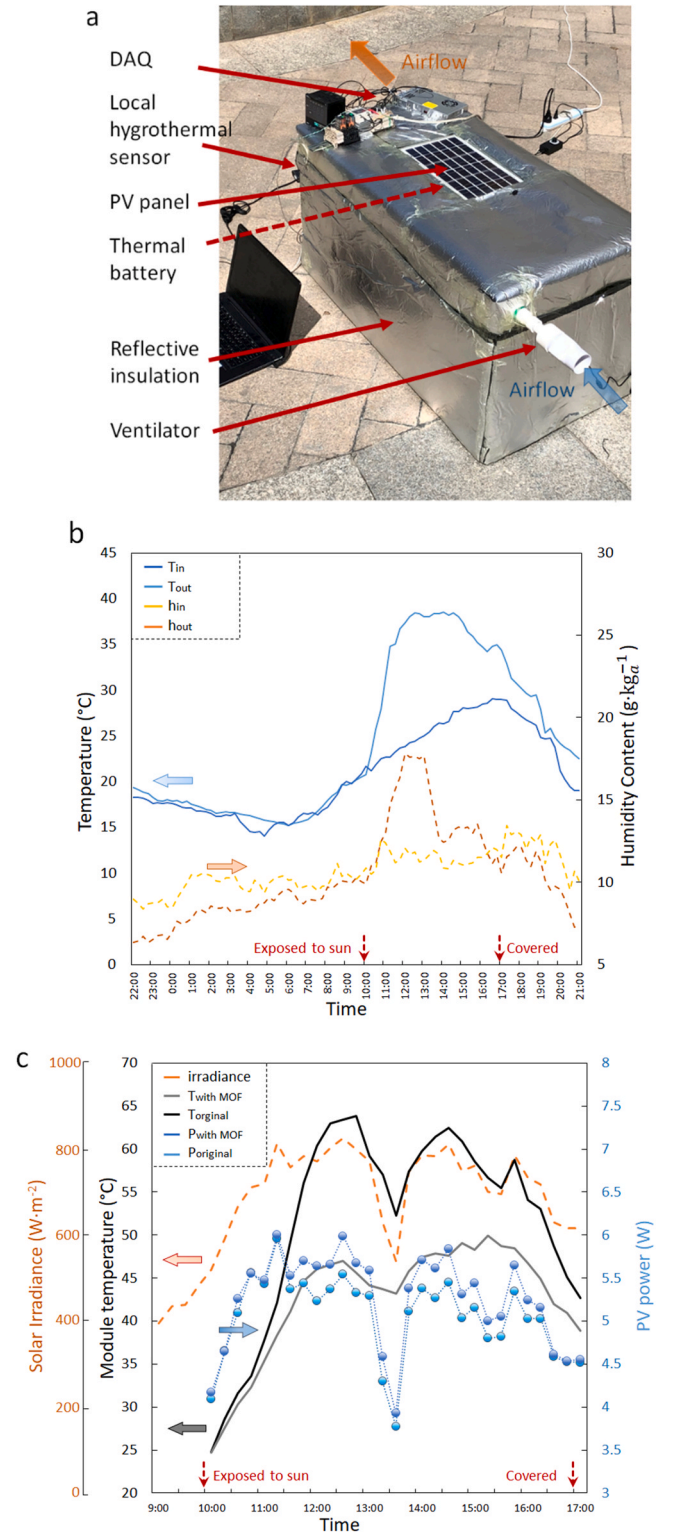

Fig. 5. Demonstration of PV thermal battery under real conditions. (a) Photo of a proof-of-concept PV panel (18 V-8 W, 697 cm^2) coated with Al-Fum of 215.8 g (~7.5 mm). The PV thermal battery was embedded in the top surface of a thermally insulated Plexiglas box, which represented the indoor environment. (b) Profiles of the inlet/outlet air conditions, ambient air. (c) Profiles of PV's rear side temperature and power output.

similar to the rear side temperature of the PV thermal battery. During the 7 h exposure to sun, the PV with thermal battery produced 4–5% more electricity than the original one (Fig. 5c). Considering the relatively low sunlight intensity (with less than 5 h between 600 W m^{-2} and 800 W m^{-2}), the result was rather acceptable.

7. Interactive design is more favorable for the investment decision

A MOF thermal battery may distinguish the scenarios of utility PV and BIPV in terms of LCOE, albeit not all competitiveness in the latter market segment can be quantitatively expressed. We can calculate the LCOE of the original PV system ($LCOE_{PV}$) and the new design with thermal battery ($LCOE_{PVTB}$).

$$\mathrm{LCOE} = \frac{\sum_{t=0}^{N} \frac{I(t)+OM(t)}{(1+r)^t}}{\sum_{t=0}^{N} \frac{E(t)}{(1+r)^t}} \tag{1}$$

Since the definition of LCOE is the cost over electricity generation over lifetime, we can obtain the maximum allowable cost of the thermal battery by equalizing $LCOE_{PV}$ and $LCOE_{PVTB}$. Beyond this cost, the investment is economically unviable.

$$\frac{\sum_{t=0}^{N} \frac{I_{PV}+OM_{PV}}{(1+r)^t}}{\sum_{t=0}^{N} \frac{E_{PV}}{(1+r)^t}} = \frac{\sum_{t=0}^{N} \frac{I_{PV}+I_{TB}+OM_{PV+}OM_{TB}}{(1+r)^t}}{\sum_{t=0}^{N} \frac{E_{PVTB}}{(1+r)^t}} \tag{2}$$

The $LCOE_{PV}$ of a BIPV project in west Europe (Paris) in 2019 was €16.7 ct kWh^{-1}, and hence the corresponding allowable cost of Al-Fum is 7.31 € kg^{-1}, assuming the discount rate is 5.2% and the project lifetime is 25 years (Supplementary Note 4).

However, this only calculated the electricity-side benefit of the design. Dewing via compression machines is a common approach for dehumidification while always at a high volume and energy penalty. If we count that, all dehumidification effects are enabled by a compression-based air-conditioner and the electricity consumed is totally generated by the PV system, the corresponding maximum allowable cost of Al-Fum would then increase to 10.38 € kg^{-1} as a result of the saved energy. This type of additional margin will be favorable for the MOF thermal battery to enter the market, especially in the early stage when the production scale will be limited. Obviously, the traditional thermal batteries will have no benefits from this added value. Considering that the energy density is the only factor for the electricity generation increase in such system, a thermal battery based on PCMs has only a maximum allowable cost of 1.57 € kg^{-1} in the same BIPV scenario.

Our calculations took into account only energy perspectives while disregarding other factors listed previously, including the space saving thanks to high compactness, the improved health conditions and prolonged building duration enabled by a MOF thermal battery. In the utility scenario, where the $LCOE_{pv}$ is lower, the allowable cost of Al-Fum also decreases, and the PV thermal battery system must compete with more alternative technology choices, such as a bifacial PV system [44], which will make the investment decision harsher.

8. Conclusion

In this study, we propose a new concept of MOF-based thermal battery to reallocate heat between PV panels and the built environment in bi-direction. Using excess moisture for discharging and waste solar thermal for charging realizes the dehumidification and PV cooling alternately. The interactive working mode can significantly benefit the maximum allowable cost of such an energy storage and transfer system to facilitate the investment decision of stakeholders along the value

chain. The design architecture and working principles demonstrated in the manuscript can be adapted to broader climates and scenarios for BIPV's market penetration as well as inspires other solar thermal management applications.

While the performance of the first field test is promising, there is still much space for improving the system and optimizing the discharging-charging process in the next studies. Under the outdoor weather conditions, Al-Fum should be able to create a cooling effect at 40 °C, nevertheless, a 10 °C higher temperature plateau was recorded. We attributed this to the thermally insulating nature of the porous adsorbents. The thermal battery should be adequately engineered so that the sorbent would not have an adverse effect on drying the air or cooling the PV. For instance, the heat transfer can be partially improved by low-cost conductive additives such as graphite and metallic substrates. Or, since less hydrophilic materials can be effective longer, the trade-off must be found between deploying more adsorbent to compromise the energy loss in low-temperature regions and increasing thermal resistance.

CRediT authorship contribution statement

F.C., C.S., and J.H.: Conceptualization. **F.C., R.L., F.N., C.S., and J.H.**: Methodology. **E.G., B.M., F.C. and F.N.**: Investigation. **E.G., B.M. and F.C.**: Writing - original draft. **E.G., B.M., F.C., R.L., F.N., C.S., J.H.**: Writing - review & editing.

Declaration of Competing Interest

The authors declare that they have no known competing financial interests or personal relationships that could have appeared to influence the work reported in this paper.

Data availability

Details about the synthesis of materials, the techno-economic models, and the data used to draw the conclusions can be found in the Supplementary Information. Requests for further information should be addressed to the corresponding authors.

Acknowledgements

F.C. acknowledges funding from the European Union's Horizon 2020 Programme under MSCA grant agreement No. 754462 and Bjarne Saxhofs Foundation. E.G., F.N. and C.S. acknowledge the CNRS, ENS, ESPCI and PSL University for financial support. B.M., F.C., R.L. and J.H. acknowledge TU/e for support.

Appendix

Large-scale synthesis of Al-Fumarate

All reactants and solvents used were purchased from commercial sources and were used without further purification.

The synthesis of Al-Fum was performed in a 30 L reactor, 709 g (6.1 mol) fumaric acid and 734 g (18.3 mol) NaOH were dissolved in 13.25 L H_2O and heated at 60 °C under stirring, until clear. A separate solution containing 2 kg (3.0 mol) of $Al_2(SO_4)_3{\cdot}18H_2O$ dissolved in 14.75 L H_2O was prepared and heated at 60 °C under stirring, until clear. The metal source solution was then added to the reactor and the mixture was heated at 60 °C, under stirring for 30 min. At the end of the reaction, the product was separated by filtration, under vacuum and left to dry at RT overnight. Subsequently, the product was washed with 10 L H_2O and 10 L EtOH (abs.) to remove any traces of unreacted metal source and ligand and recovered again by filtration. Finally, the purified powder was dried at 100 °C for 10 h, under vacuum. Product mass = 1.4 kg; Space-Time Yield ~ 2250 kg m^{-3} day^{-1}.

Material characterization

Al-Fum was characterized by various techniques to ensure the purity of the product (Fig. S1). PXRD FT-IR analysis shows characteristic peaks of Al-Fum crystal structure. The thermogravimetric analysis showed two major weight losses; one at T ≤ 100 °C due to the removal of adsorbed solvent molecules and a second one at T = 435 °C, corresponding to the degradation of the organic part and the collapse of the structure, leaving oxide/hydroxide residues. The measured weight losses are in agreement with the chemical structure of Al-Fum ($Al(OH)(C_4O_4H_2){\cdot}xH_2O$ (x~ 4)). A specific surface of 1000 m^2 g^{-1} was obtained from N_2 sorption measurement (77 K) in agreement with the reported values [30]. Synthesis of other MOFs used in the laboratory test can refer to Supplementary Note 1, material characterization follows the similar protocol.

Coating procedure

Selected MOF powders were dispersed in deionized water (mass ratio 1:1.8) with vigorous stirring for 15 min followed by supersonic treatment for 10 min. A binder of organic silicone (dry mass ratio ~40%) was added to the suspension with continuous stirring (mass ratio 0.3:1 and 0.15:1 for the lab test samples and the outdoor test sample, respectively). The coating was carried out manually with a pipette on the rear side of commercial PV panels [45]. Low-rise aluminum fins were attached as support for the outdoor test sample to increase the thermal conductivity. After natural drying for 1 h, an infrared lamp was used for curing the coating layer at 85 °C for 2 h.

Appendix A. Supporting information

Supplementary data associated with this article can be found in the online version at doi:10.1016/j.nanoen.2021.106224.

References

[1] U. von der Leyen, A Union that strives for more – My agenda for Europe; Political Guidelines for the next European Commission 2019–2024, 16 July 2019.
[2] C. Breyer, D. Bogdanov, A. Gulagi, A. Aghahosseini, L.S.N.S. Barbosa, O. Koskinen, M. Barasa, U. Caldera, S. Afanasyeva, M. Child, J. Farfan, P. Vainikka, On the role of solar photovoltaics in global energy transition scenarios, Prog. Photovolt. 25 (2017) 727–745.
[3] Solar Power Europe, Global market outlook for solar power 2019–2023, July 2019, ISBN 978-90-82-71432-6.
[4] A. Jäger-Waldau, PV Status Report 2019 (Publications Office, European Union, 2019). Luxembourg, 2019.
[5] B.P. Jelle, C. Breivik, H.D. Røkenes, Building integrated photovoltaic products: a state-of-the-art review and future research opportunities, Sol. Energy Mater. Sol. Cells 100 (2012) 69–96.
[6] P. Defaix, W. van Sark, E. Worrell, E. de Visser, Technical potential for photovoltaics on buildings in the EU-27, Sol. Energy 86 (2012) 2644–2653.
[7] C. Ballif, L.-E. Perret-Aebi, S. Lufkin, E. Rey, Integrated thinking for photovoltaics in buildings, Nat. Energy 3 (2018) 438–444.
[8] A.K. Shukla, K. Sudhakar, P. Baredar, Recent advancement in BIPV product technologies: a review, Energy Build. 140 (2017) 188–195.
[9] E. Biyik, M. Araz, A. Hepbasli, M. Shahrestani, R. Yao, L. Shao, E. Essah, A. C. Oliveira, T. del Caño, E. Rico, J.L. Lechón, L. Andrade, A. Mendes, Y.B. Atlı, A key review of building integrated photovoltaic (BIPV) systems, Eng. Sci. Technol. Int. J. 20 (2017) 833–858.
[10] P. Wilkinson, K.R. Smith, S. Beevers, C. Tonne, T. Oreszczyn, Energy, energy efficiency, and the built environment, Lancet 370 (2007) 1175–1187.
[11] X. Liu, X. Wang, F. Kapteijn, Water and metal−organic frameworks: from interaction toward utilization, Chem. Rev. 120 (2020) 8303–8377.
[12] N. Hanikel, M.S. Prévot, O.M. Yaghi, MOF water harvesters, Nat. Nanotechnol. 15 (2020) 348–355.
[13] P.G. Mileo, K.H. Cho, J. Park, S. Devautour-Vinot, J.-S. Chang, G. Maurin, Unraveling the water adsorption mechanism in the mesoporous MIL-100 (Fe) metal−organic framework, J. Phys. Chem. C 123 (2019) 23014–23025.
[14] A.J. Rieth, A.M. Wright, M. Dincă, Kinetic stability of metal-organic frameworks for corrosive and coordinating gas capture, Nat. Rev. Mater. 4 (2019) 708–725.
[15] G. Mouchaham, F.S. Cui, F. Nouar, V. Pimenta, J.-S. Chang, C. Serre, Metal-organic frameworks and water: 'from old enemies to friends'? Trends Chem. 2 (2020) 990–1003.
[16] J.D. Evans, B. Garai, H. Reinsch, W. Li, S. Dissegna, V. Bon, I. Senkovska, R. A. Fischer, S. Kaskel, C. Janiak, N. Stock, D. Volkmer, Metal–organic frameworks in Germany: from synthesis to function, Coord. Chem. Rev. 380 (2019) 378–418.

[17] S. Wang, C. Serre, Toward green production of water-stable metal-organic frameworks based on high-valence metals with low toxicities, ACS Sustain. Chem. Eng. 7 (2019) 11911–11927.
[18] R. van Alebeek, L. Scapino, M.A.J.M. Beving, M. Gaeini, C.C.M. Rindt, H. A. Zondag, Investigation of a household-scale open sorption energy storage system based on the zeolite 13X/water reacting pair, Appl. Therm. Eng. 139 (2018) 325–333.
[19] C. Wang, L. Hua, H. Yan, B. Li, Y. Tu, R. Wang, A thermal management strategy for electronic devices based on moisture sorption-desorption processes, Joule 4 (2020) 1–13.
[20] S. Pu, J. Fu, Y. Liao, L. Ge, Y. Zhou, S. Zhang, S. Zhao, X. Liu, X. Hu, K. Liu, J. Chen, Promoting energy efficiency via a self-adaptive evaporative cooling hydrogel, Adv. Mater. 32 (2020), 1907307.
[21] R. Li, Y. Shi, M. Wu, S. Hong, P. Wang, Photovoltaic panel cooling by atmospheric water sorption–evaporation cycle, Nat. Sustain. 3 (2020) 636–643.
[22] S. Pu, Y. Liao, K. Chen, J. Fu, S. Zhang, L. Ge, G. Conta, S. Bouzarif, T. Chen, X. Hu, K. Liu, J. Chen, Thermogalvanic hydrogel for synchronous evaporative cooling and low-grade heat energy harvesting, Nano Lett. 20 (2020) 3791–3797.
[23] J. Xu, J. Chao, T. Li, T. Yan, S. Wu, M. Wu, B. Zhao, R. Wang, Near-zero-energy smart battery thermal management enabled by sorption energy harvesting from air, ACS Cent. Sci. 6 (2020) 1542–1554.
[24] T. Ma, H. Yang, Y. Zhang, L. Lu, X. Wang, Using phase change materials in photovoltaic systems for thermal regulation and electrical efficiency improvement: a review and outlook, Renew. Sustain. Energy Rev. 43 (2015) 1273–1284.
[25] I.M. Peters, C.D.R. Gallegos, S.E. Sofia, T. Buonassisi, The value of efficiency in photovoltaics, Joule 3 (2019) 2732–2747.
[26] J. Vimpari, S. Junnila, Estimating the diffusion of rooftop PVs: a real estate economics perspective, Energy 172 (2019) 1087–1097.
[27] M. Gaab, N. Trukhan, S. Maurer, R. Gummaraju, U. Müller, The progression of Al-based metal-organic frameworks - from academic research to industrial production and applications, Microporous Mesoporous Mater. 157 (2012) 131–136.
[28] E. Leung, U. Müller, G. Cox, H. Mattenheimer, S. Blei, EP Patentanmeldung 10183283.0, 2010.
[29] S. Cui, P. Stabat, D. Marchio, Numerical simulation of wind-driven natural ventilation: effects of loggia and facade porosity on air change rate, Build. Environ. 106 (2016) 131–142.
[30] E. Alvarez, N. Guillou, C. Martineau, B. Bueken, B. Van de Voorde, C. Le Guillouzer, P. Fabry, F. Nouar, F. Taulelle, D. de Vos, J.S. Chang, K.H. Cho, N. Ramsahye, T. Devic, M. Daturi, G. Maurin, C. Serre, The structure of the aluminum fumarate metal–organic framework A520, Angew. Chem. Int. Ed. 54 (2015) 3664–3668.
[31] H. Reinsch, M.A. Van der Veen, B. Gil, B. Marszalek, T. Verbiest, D. De Vos, N. Stock, Structures, sorption characteristics, and nonlinear optical properties of a new series of highly stable aluminum MOFs, Chem. Mater. 25 (2013) 17–26.
[32] A. Cadiau, J.S. Lee, D. Damasceno Borges, P. Fabry, T. Devic, M.T. Wharmby, C. Martineau, D. Foucher, F. Taulelle, C.-H. Jun, Y.K. Hwang, N. Stock, M.F. De Lange, F. Kapteijn, J. Gascon, G. Maurin, J.S. Chang, C. Serre, Design of hydrophilic metal organic framework water adsorbents for heat reallocation, Adv. Mater. 27 (2015) 4775–4780.
[33] S. Cui, A. Marandi, G. Lebourleux, M. Thimon, M. Bourdon, C. Chen, M.I. Severino, V. Steggles, F. Nouar, C. Serre, Heat properties of a hydrophilic carboxylate-based MOF for water adsorption applications, Appl. Therm. Eng. 161 (2019), 114135.
[34] A. Lamaire, J. Wieme, A.E.J. Hoffman, V.V. Speybroeck, Atomistic insight in the flexibility and heat transport properties of the stimuli-responsive metal-organic framework MIL-53(Al) for water-adsorption applications using molecular simulations, Faraday Discuss. 225 (2021) 301–323.
[35] C. Amy, H.R. Seyf, M.A. Steiner, D.J. Friedman, A. Henry, Thermal energy grid storage using multi-junction photovoltaics, Energy Environ. Sci. 12 (2019) 334–343.
[36] K. Wang, M. Antonio, A.M. Pantaleo, M. Herrando, M. Faccia, I. Pesmazoglou, B. M. Franchetti, C.N. Markides, Spectral-splitting hybrid PV-thermal (PVT) systems for combined heat and power provision to dairy farms, Renew. Energy 159 (2020) 1047–1065.
[37] J. Park, T. Kim, S.-B. Leigh, Application of a phase-change material to improve the electrical performance of vertical-building-added photovoltaics considering the annual weather conditions, Sol. Energy 105 (2014) 561–574.
[38] A. Hasan, J. Sarwar, H. Alnoman, S. Abdelbaqi, Yearly energy performance of a photovoltaic-phase change material (PV-PCM) system in hot climate, Sol. Energy 146 (2017) 417–429.
[39] Y. Zhou, S. Zheng, Z. Liu, T. Wen, Z. Ding, J. Yan, G. Zhang, Passive and active phase change materials integrated building energy systems with advanced machine-learning based climate-adaptive designs, intelligent operations, uncertainty-based analysis and optimisations: a state-of-the-art review, Renew. Sustain. Energy Rev. 130 (2020), 109889.
[40] V. Kashyap, S. Sakunkaewkasem, P. Jafari, M. Nazari, B. Eslami, S. Nazifi, P. Irajizad, M.D. Marquez, T.R. Lee, H. Ghasemi, Full spectrum solar thermal energy harvesting and storage by a molecular and phase-change hybrid material, Joule 3 (2019) 3100–3111.
[41] D.K. Nandakumar, S.K. Ravi, Y. Zhang, N. Guo, C. Zhang, S.C. Tan, A super hygroscopic hydrogel for harnessing ambient humidity for energy conservation and harvesting, Energy Environ. Sci. 11 (2018) 2179–2187.
[42] R.G. AbdulHalim, P.M. Bhatt, Y. Belmabhkhout, A. Shkurenko, K. Adil, L. J. Barbour, M. Eddaoudi, A fine-tuned Metal–Organic Framework for autonomous indoor moisture control, J. Am. Chem. Soc. 139 (2017) 10715–10722.
[43] R.C.G.M. Loonen, M. Trčka, D. Cóstola, J.L.M. Hensen, Climate adaptive building shells: state-of-the-art and future challenges, Renew. Sustain. Energy Rev. 25 (2013) 483–493.
[44] R. Kopecek, J. Libal, Towards large-scale deployment of bifacial photovoltaics, Nat. Energy 3 (2018) 443–444.
[45] S. Cui, M. Qin, A. Marandi, V. Steggles, S. Wang, X. Feng, F. Nouar, C. Serre, Metal-organic frameworks as advanced moisture sorbents for energy-efficient high temperature cooling, Sci. Rep. 8 (2018) 15284.

Supplementary Information

Moisture-participating MOF thermal battery for heat reallocation between indoor environment and building-integrated photovoltaics

Effrosyni Gkaniatsou[a], Bin Meng[b], Frédéric Cui[b,c*], Roel Loonen[b],

Farid Nouar[a], Christian Serre[a*], Jan Hensen[b*]

[a] Institut des Matériaux Poreux de Paris, FRE 2000 CNRS, Ecole Normale Supérieure, Ecole Supérieure de Physique et de Chimie Industrielles de Paris, PSL Research University, 75005 Paris, France

[b] Department of the Built Environment, Eindhoven University of Technology, P O. Box 513, 5600 MB Eindhoven, the Netherlands

[c] Department of Civil Engineering, Technical University of Denmark, Brovej Building 118, DK-2800 Kgs. Lyngby, Denmark

Email : f.s.cui@tue.nl ; christian.serre@espci.fr, j.hensen@tue.nl

This file includes:

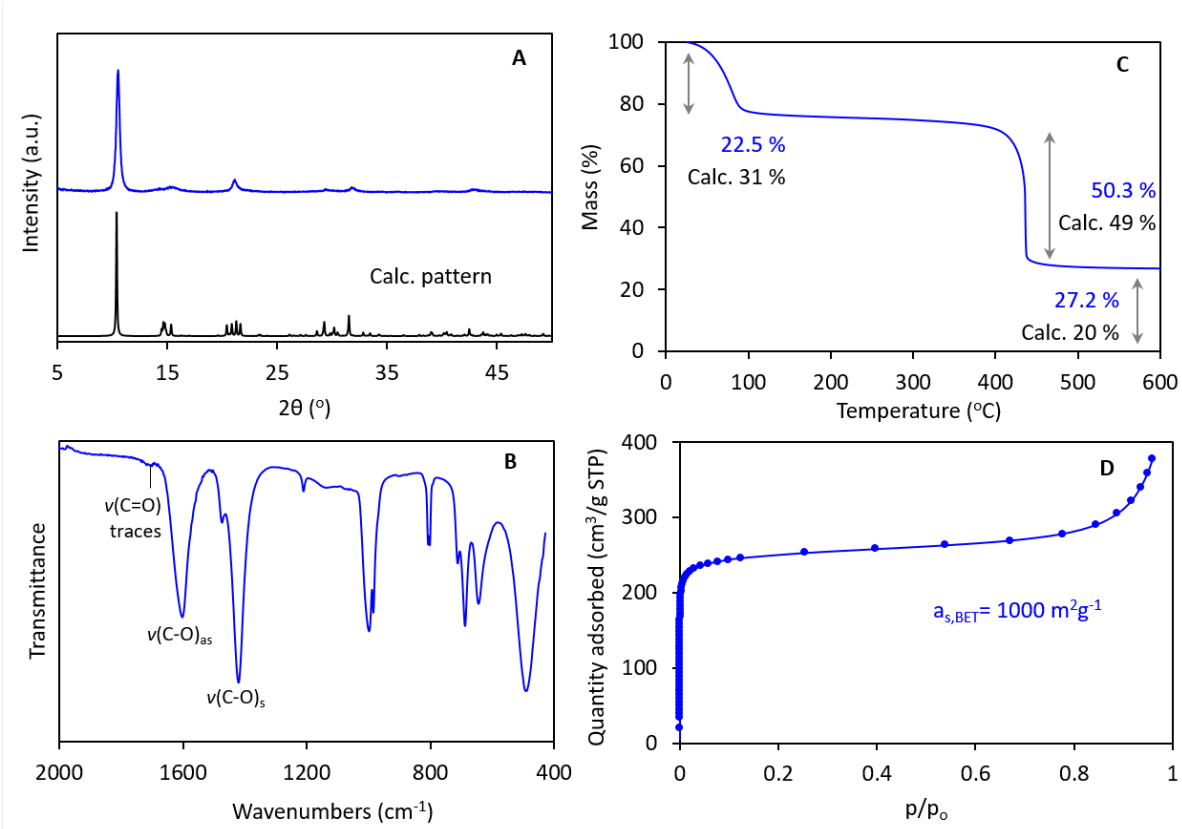

Figure S1-1. Al-Fumarate characterizations. a, PXRD pattern (λ= 1.54 Å); **b,** FT-IR spectrum; **c,** TGA curve, measured under O2 flow and with a heating rate of 3 °C/min and **d,** N_2 sorption isotherm; sample activation at 200 °C/16 h, under secondary vacuum.

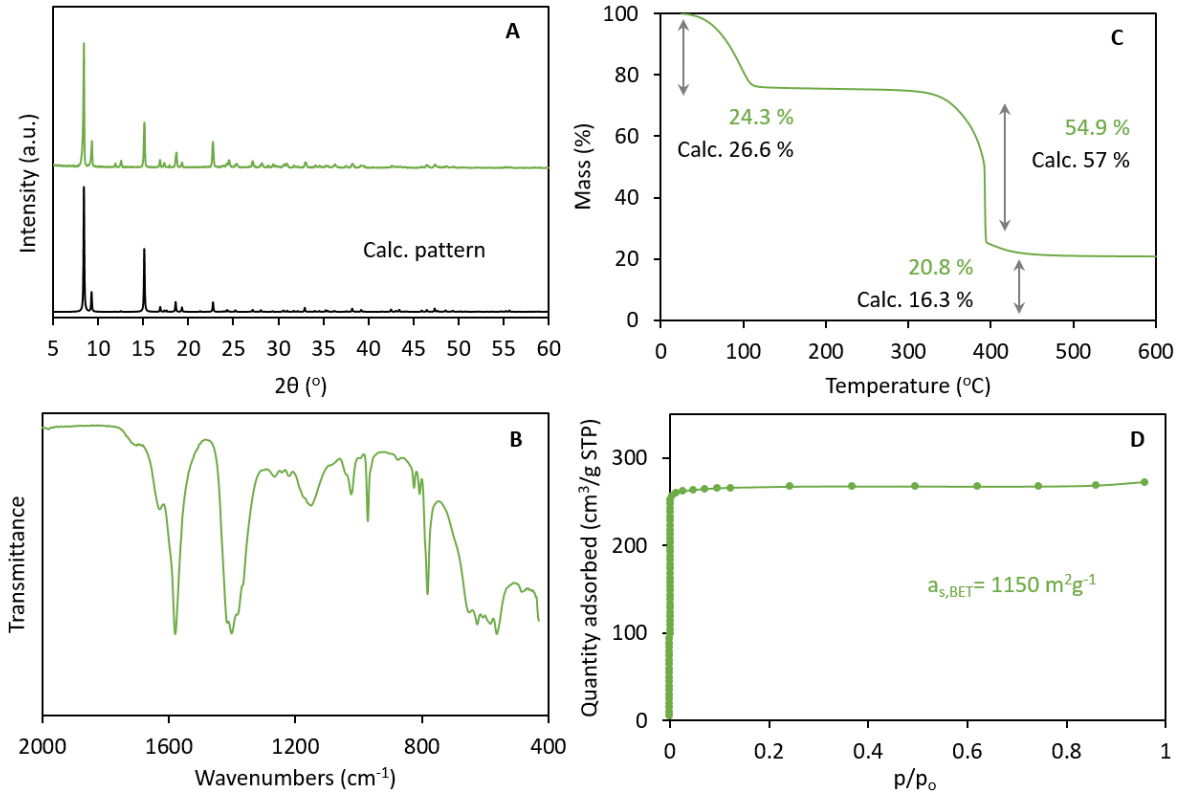

Figure S2-2. MIL-160(Al) characterizations. a, PXRD pattern (λ= 1.54 Å); **b,** FT-IR spectrum; **c,** TGA curve, measured under O_2 flow and with a heating rate of 3 °C/min; Percentages were calculated based on the formula $Al(OH)(C_6O_5H_2)\cdot xH_2O$ (x~4)[2] and **d,** N_2 sorption isotherm; sample activation at 200 °C/5 h, under secondary vacuum.

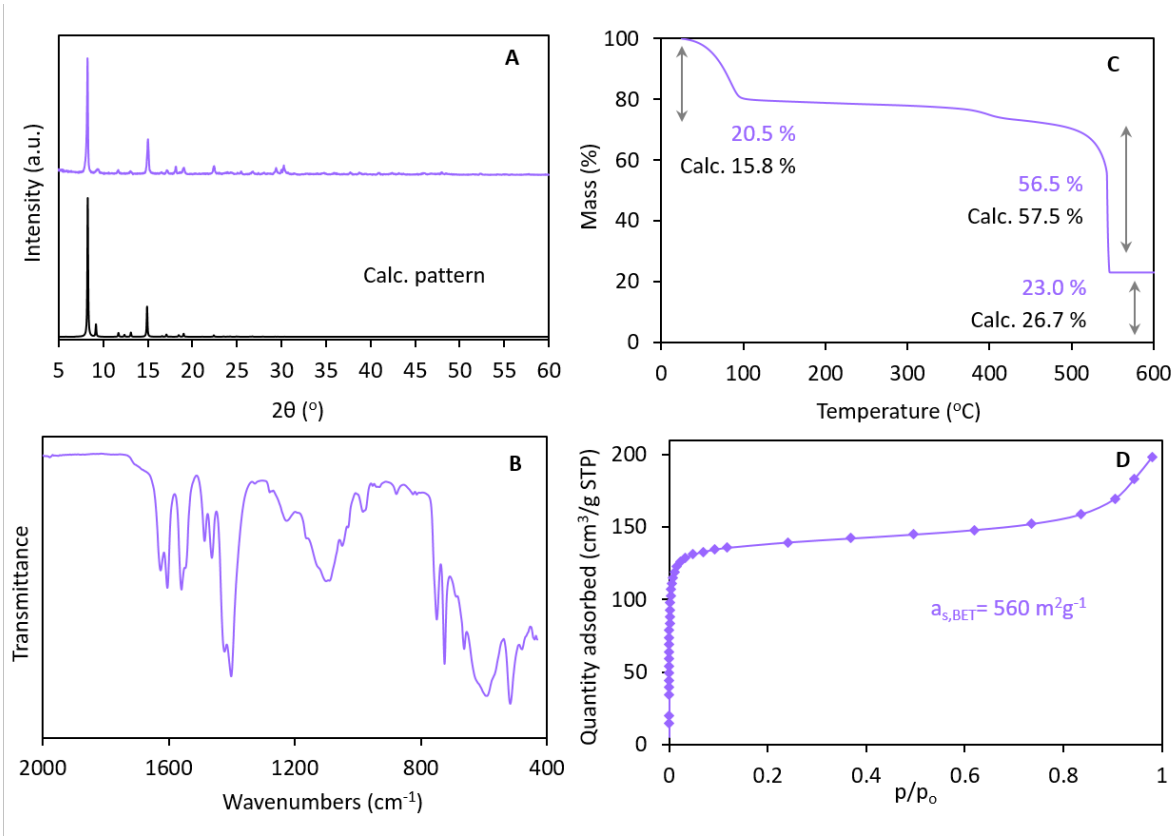

Figure S1-3. CAU-10-H characterizations. a, PXRD pattern (λ= 1.54 Å); **b,** FT-IR spectrum; **c,** TGA curve, measured under O_2 flow and with a heating rate of 3 °C/min; Percentages were calculated based on the formula $Al(OH)(C_8O_4H_4)]\cdot xH_2O$ (x~2.5)[3] and **d,** N_2 sorption isotherm; sample activation at 150 °C/16 h, under secondary vacuum.

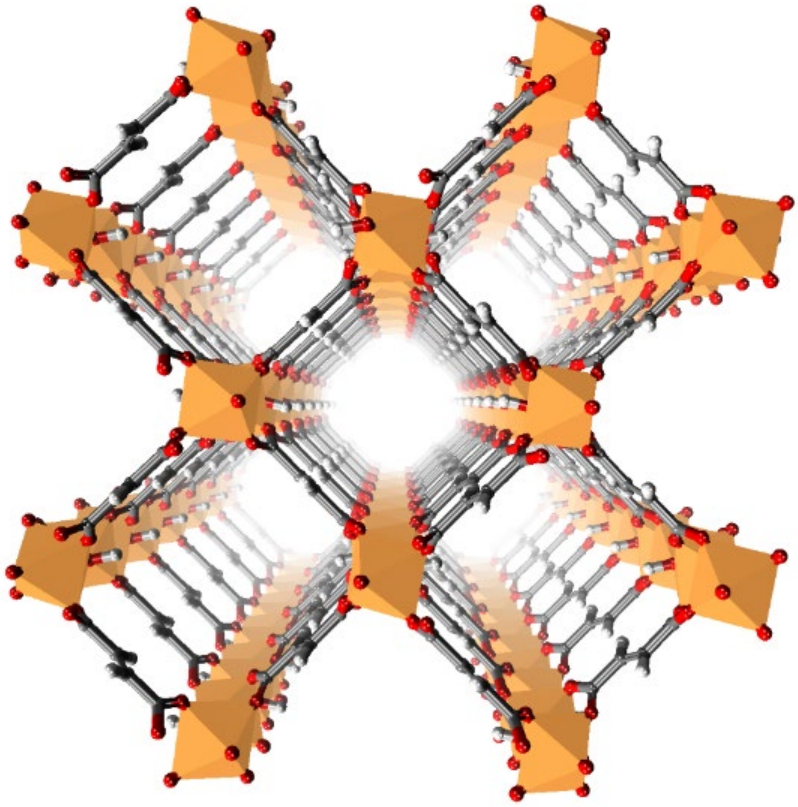

Figure S2. View along the a-axis of the Al Fum's structure. Al octahedral orange, O red, C gray. Hydrogen atoms have been omitted for clarity. The size of one-dimensional channels is 5.7 × 6.0 Å.

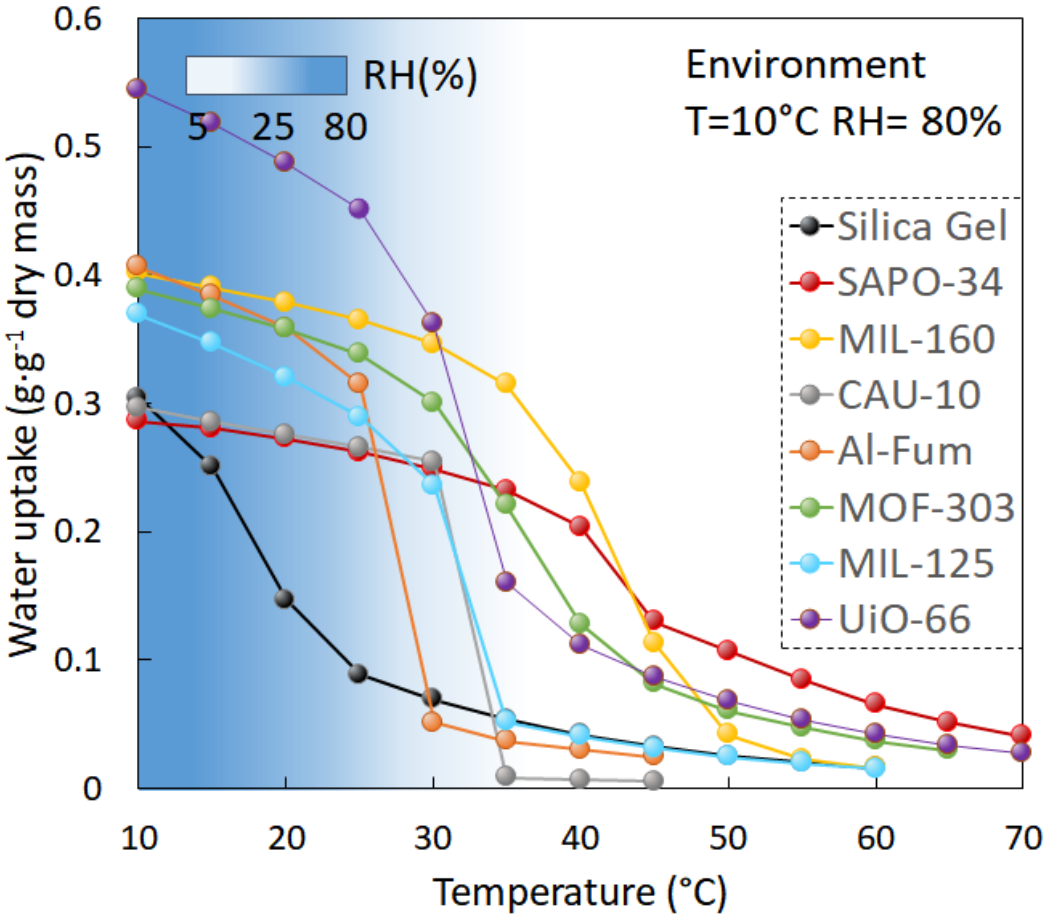

Figure S3. Isobaric heating of thermal batteries constructed with typical MOFs, zeolite and silica gel at a winter day condition of 10°C, 80%RH.

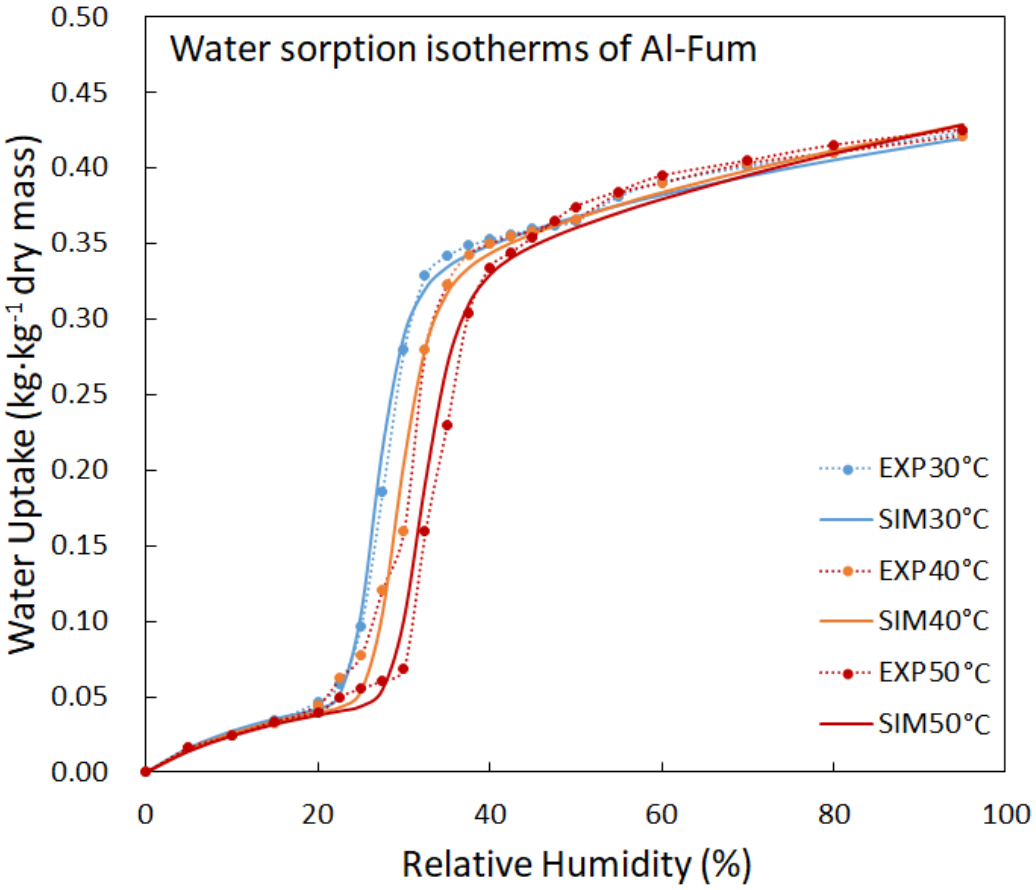

Figure S4. Measured and simulated water sorption isotherms of Al-Fum at different temperatures.

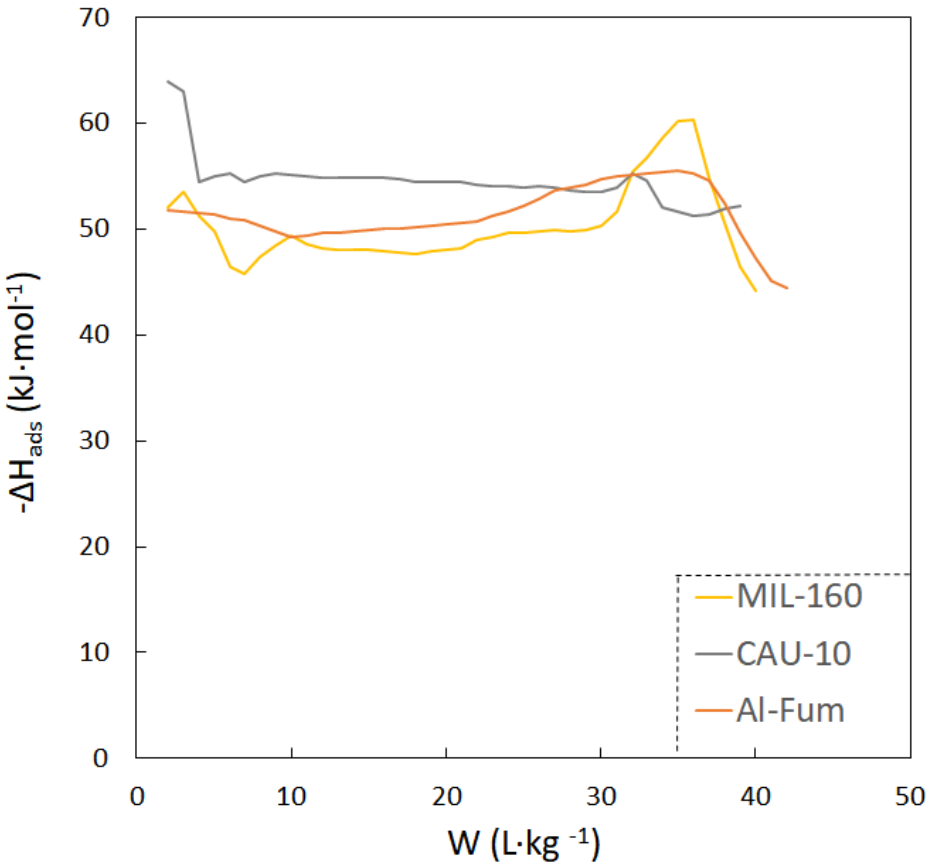

Figure S5. Isosteric enthalpy of adsorption. MIL-160, CAU-10, Al-Fum.

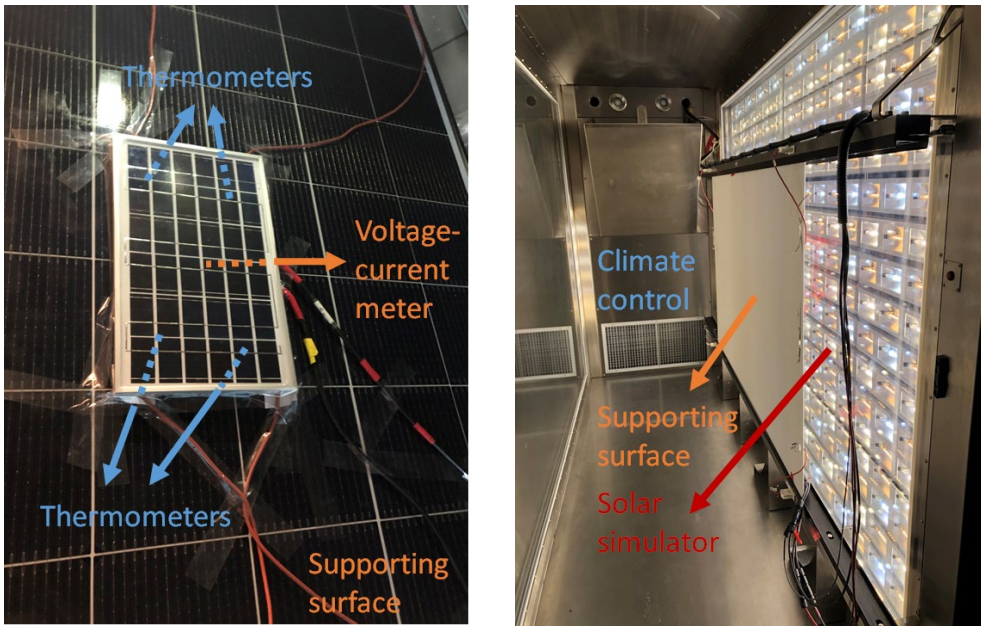

Figure S6. Laboratory set-up of PV cooling performance test.

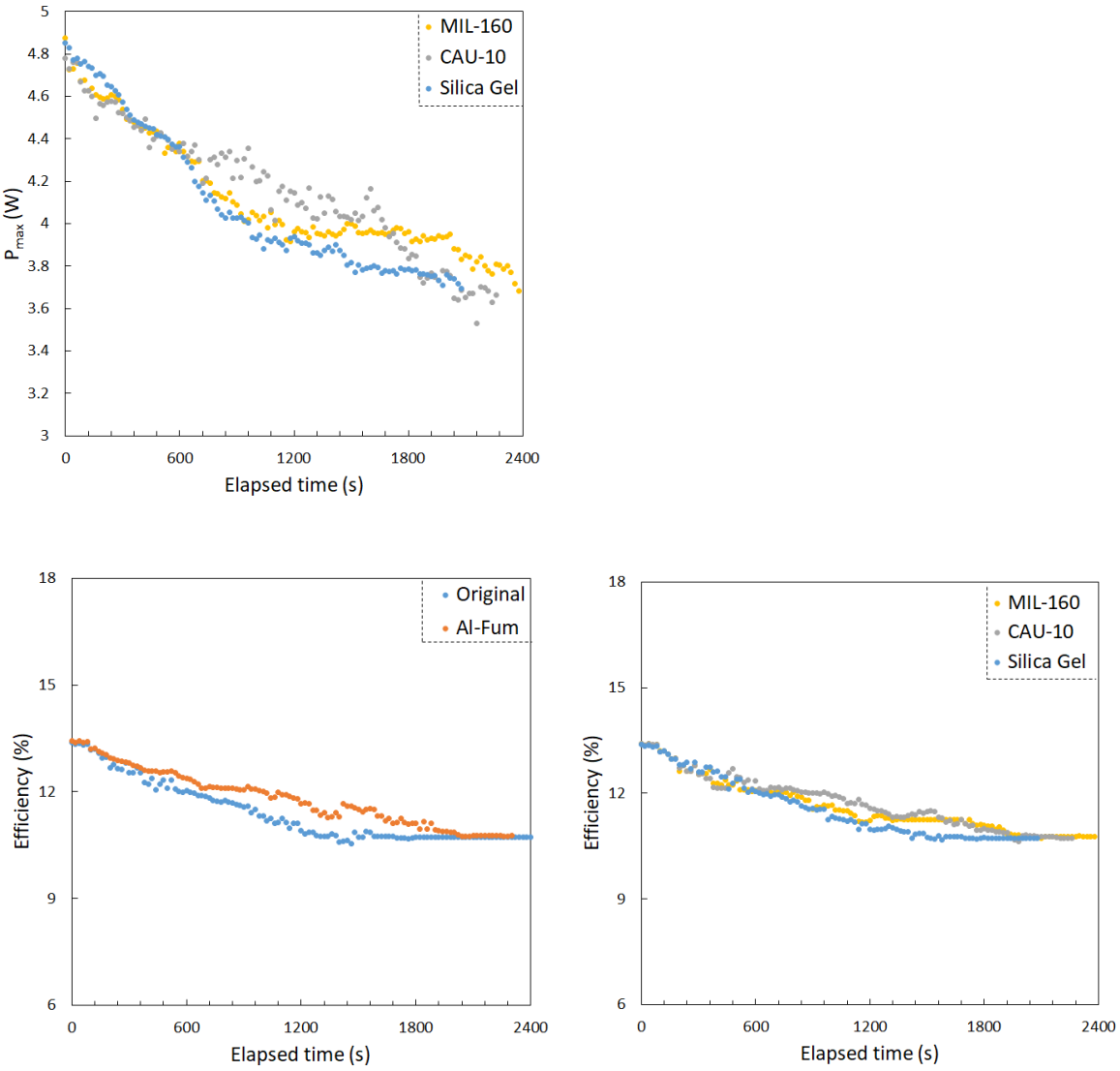

Figure S7. Electricity power output and efficiency of the PV with sorption thermal battery installed.

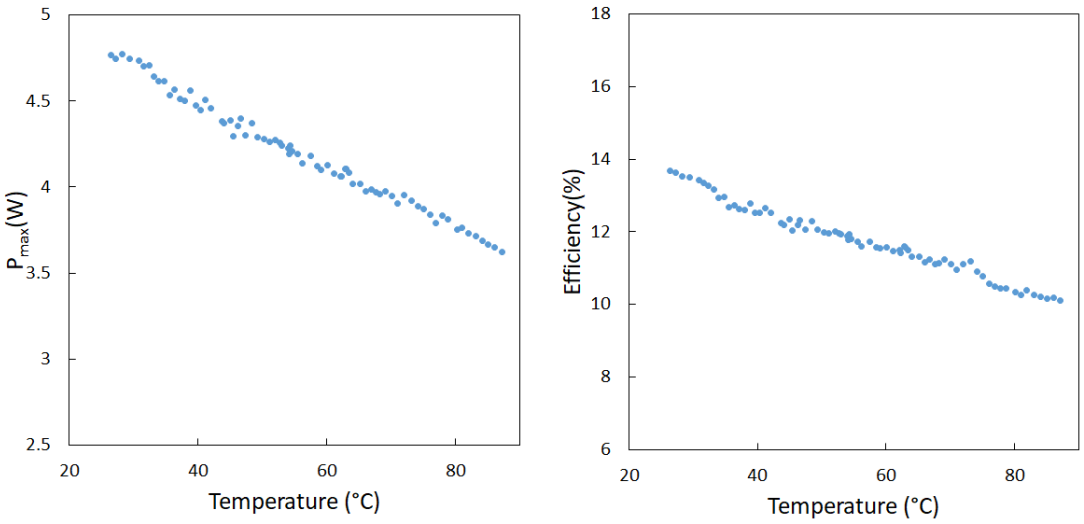

Figure S8. PV characteristics of the original panel in function of temperature under 1 kW·m^{-2}.

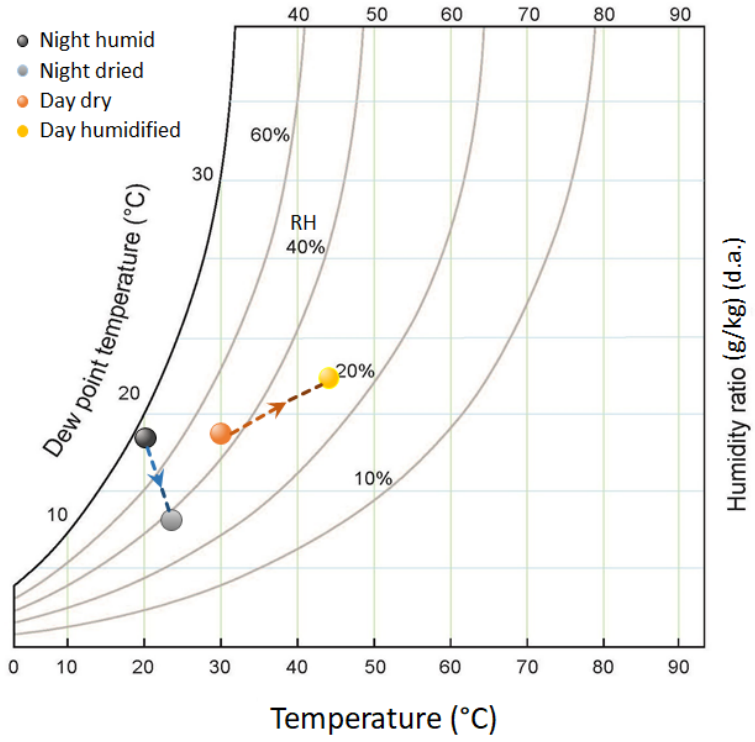

Figure S9. Psychrometric chart of the indoor/outdoor airflow that contacted with MOF thermal battery. Air was dried at night and humidified at daytime.

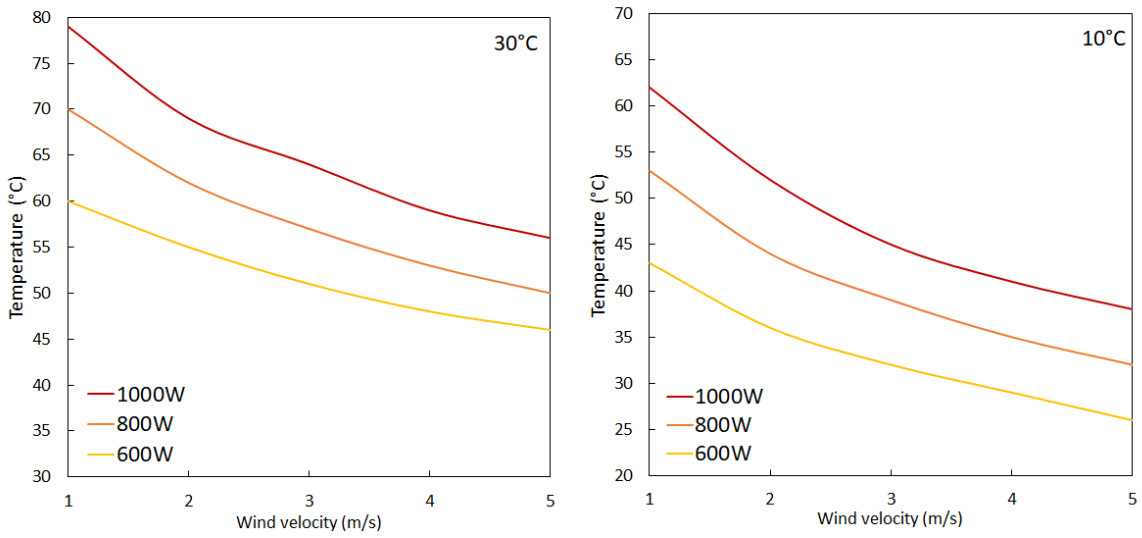

Figure S10. Temperature profiles of original PV at various solar radiation.

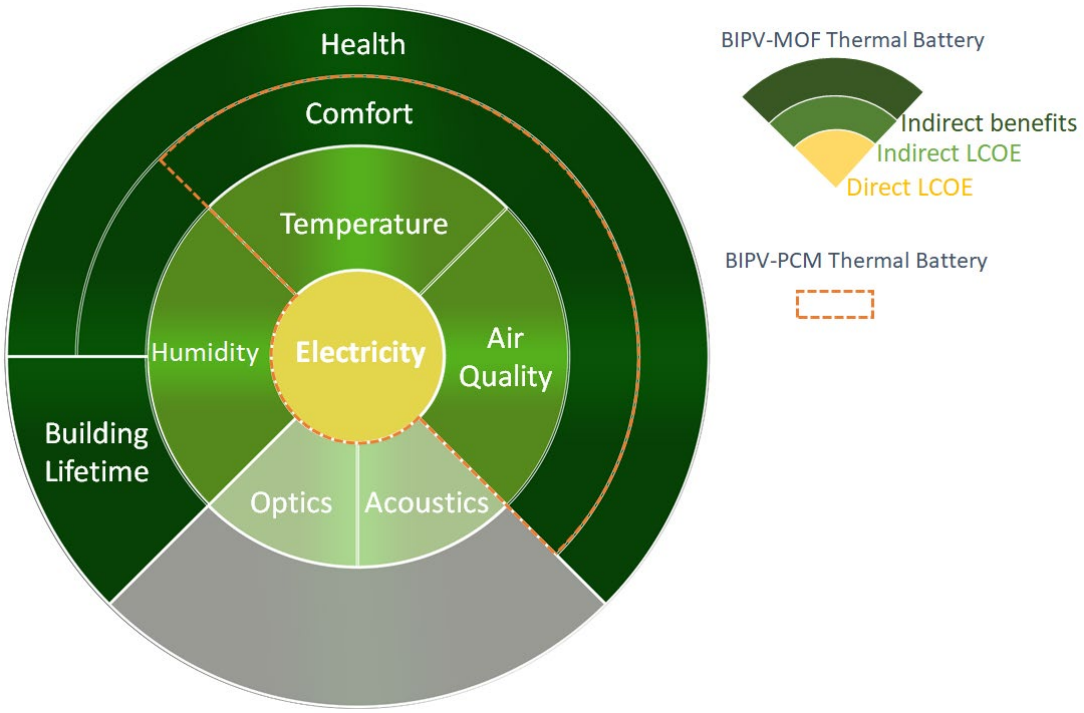

Figure S11. Interaction between the PV thermal battery and the built environment. The three circles represent the economic effects of thermal battery on the PV and building metrics with different degree from inside to outside. Increasing electricity generation can have direct impact on the calculation of LCOE; enhancing performance on building physics can be translated to energy saving or economic benefits in other types; improving the built environment can prevent unacceptable living conditions occurring or have advantages not easily to be quantified. Opaque regions exhibit the involved building metrics in the MOF thermal battery system and the translucent regions for the non-involved aspects. Inside the orange frame is the functioning of a PCM thermal battery system.

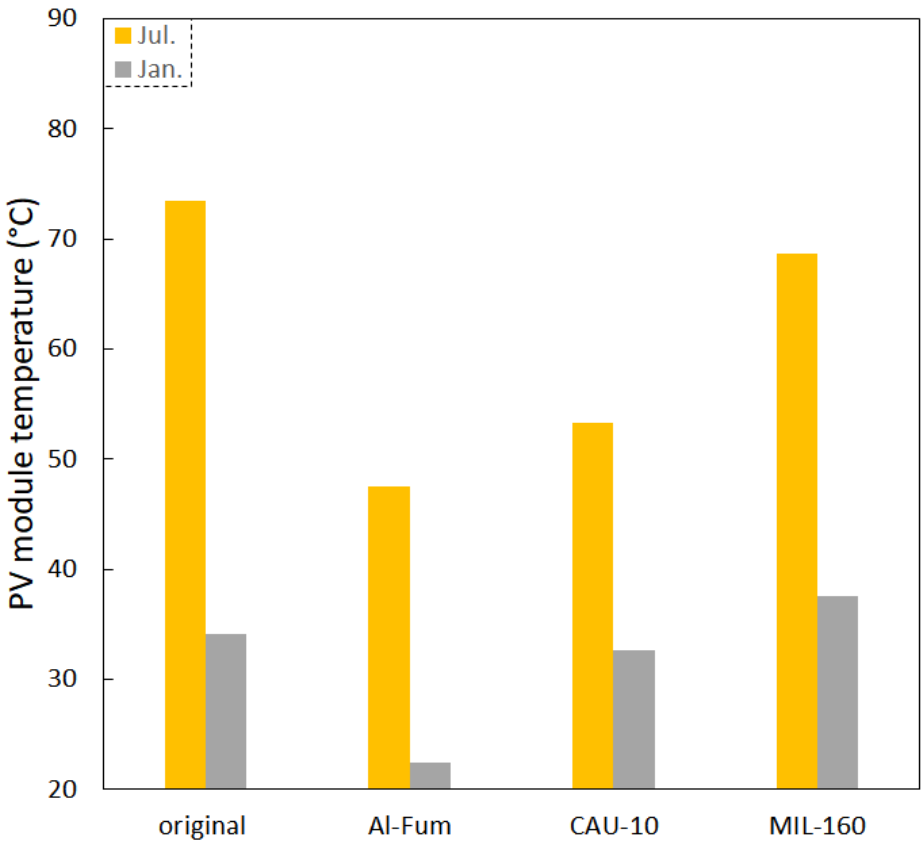

Figure S12. PV module temperature at peak irradiance in Paris with various MOF thermal batteries in representative summer and winter days.

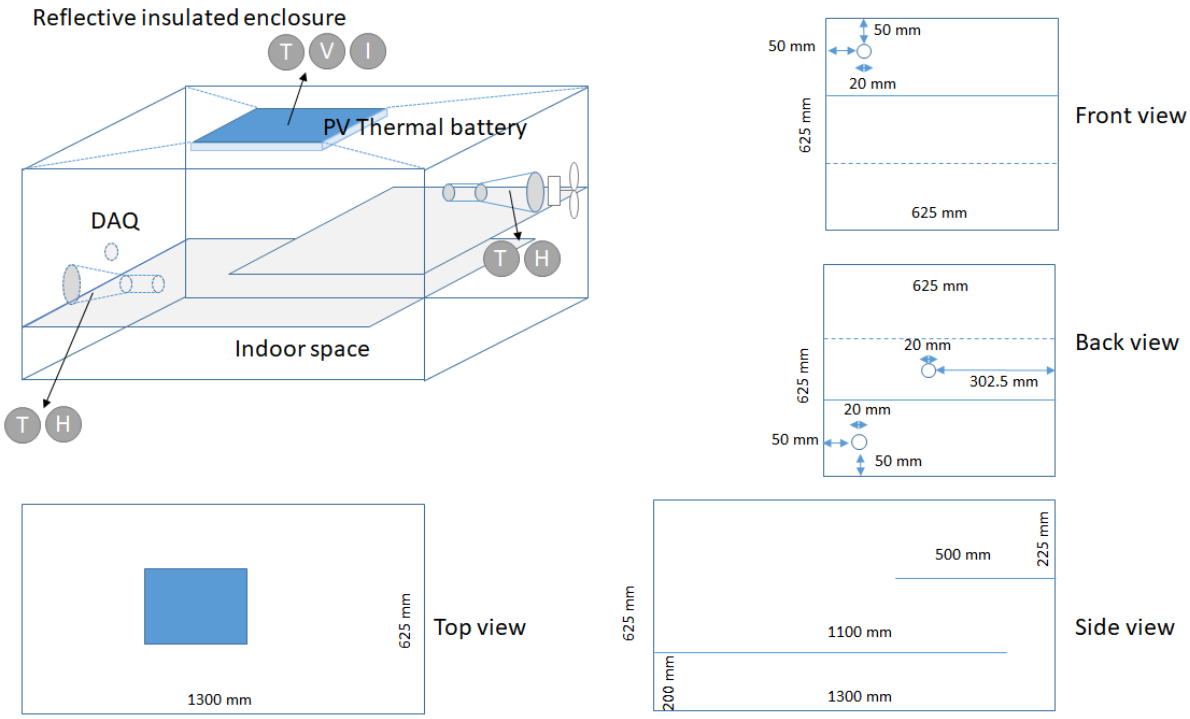

Figure S13. Outdoor test set-up. Schematic illustration of the reflective insulated enclosure embedded with a PV thermal battery. T: thermometer. H: hygrometer. V-I: voltage-current meter

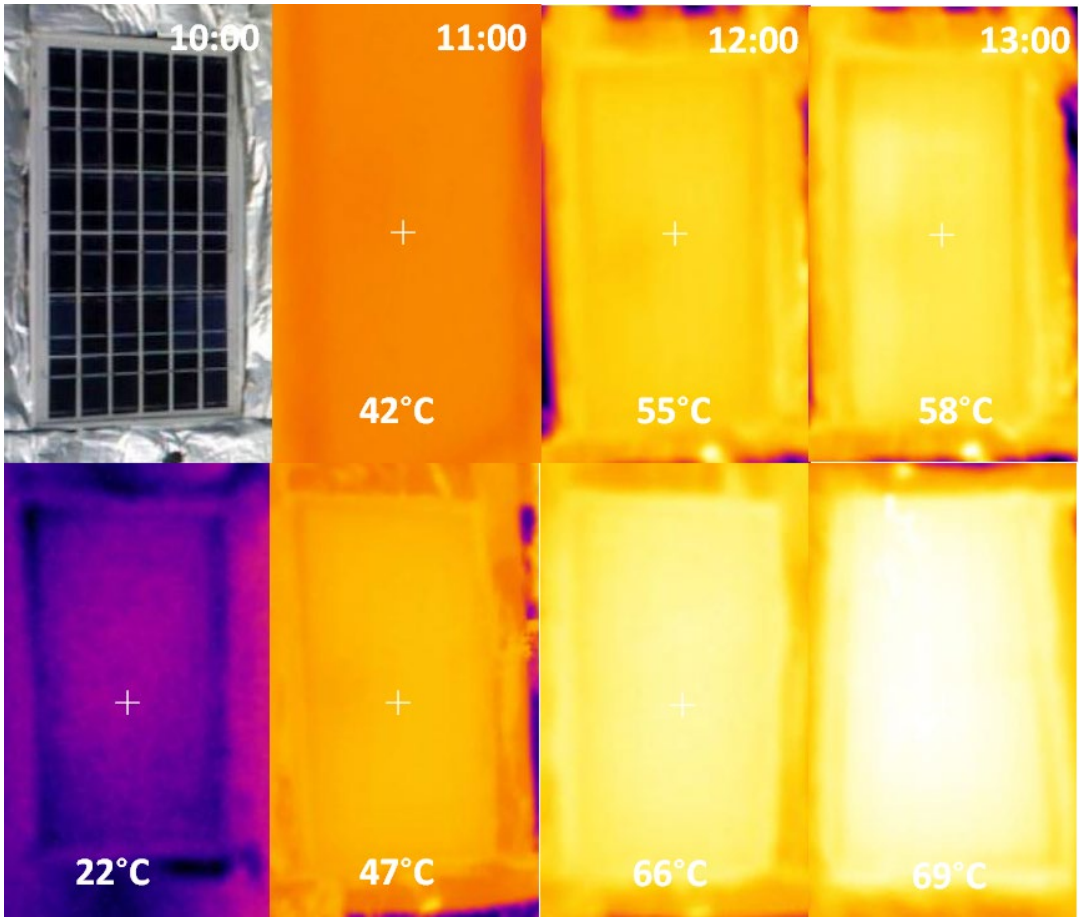

Figure S14. IR images of the original PV panel (below) and with the thermal battery (upper) in field test.

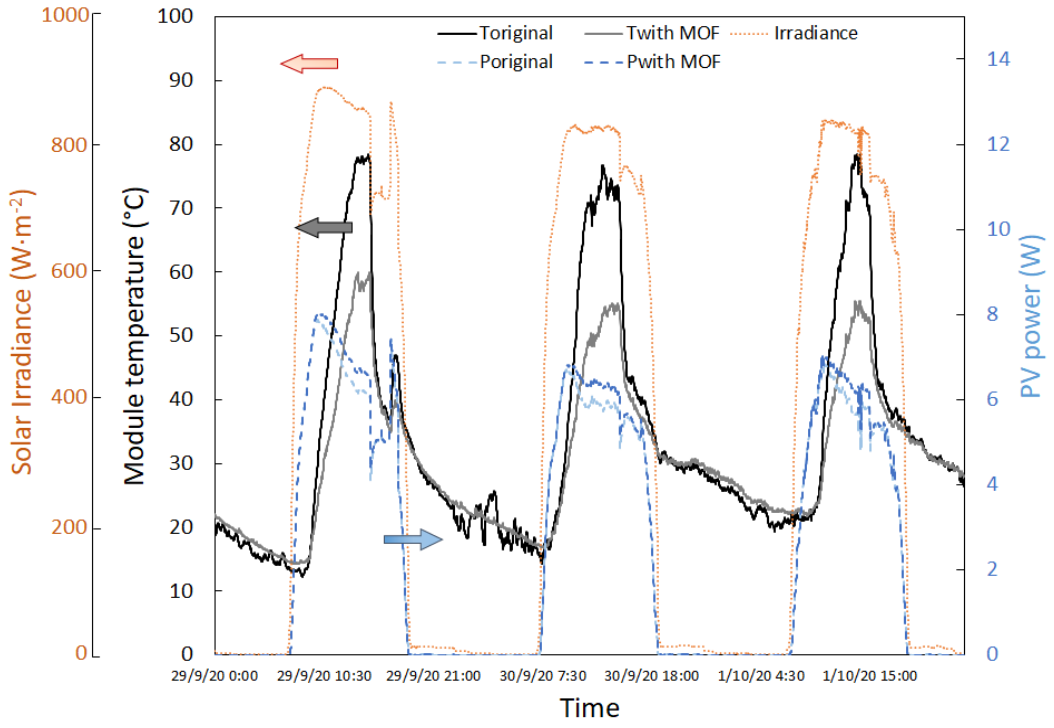

Figure S15. **Field test results in consecutive days.** The electricity generation differences between the samples with and without MOF in the three days were 4.3%, 4.9% and 3.7%, respectively.

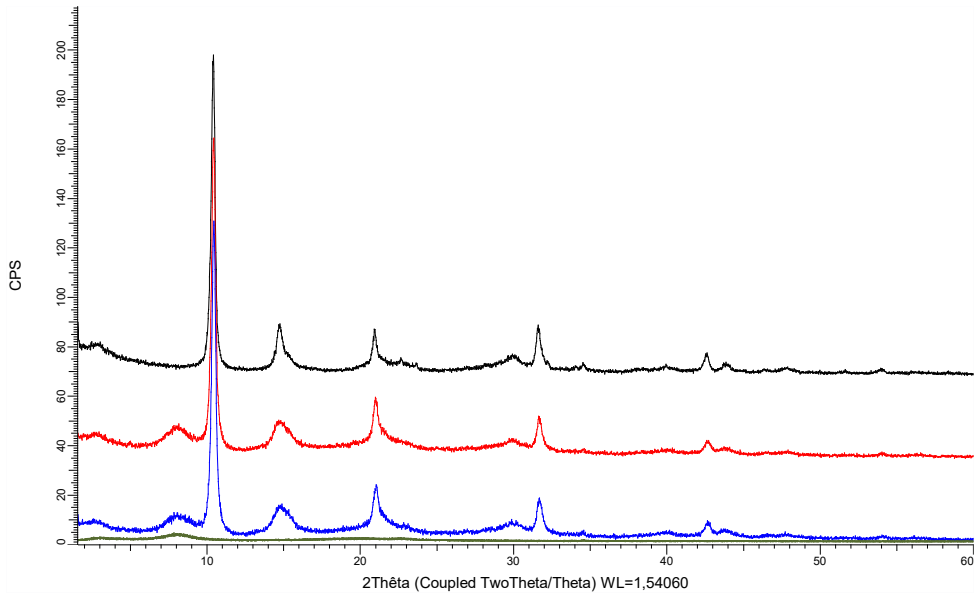

Figure S16. **PXRD of Al-Fum thermal battery.** Black: Al-Fum powder after 6 months hygrothermal tests. Red: newly shaped Al-Fum thermal battery. Blue: Shaped Al-Fum thermal battery after tests of 6 months.

Supplementary Note 1: Materials and Characterization

1.1 Large-scale synthesis of MIL-160

MIL-160 was prepared by scaling-up the reported procedure [1]. In a 30 L reactor, 1 Kg (6.2 mol) $Al(OH)(CH_3COO)_2$ and 1 Kg (6.4 mol) 2,5-furandicarboxylic acid were dissolved in 6.4 L H_2O and refluxed for 24 h. The product was collected, washed and dried overnight. Product mass = 1.4 Kg; Yield = 87.5 %.

1.2 Large-scale synthesis of CAU-10

CAU-10-H was synthesized based on the reported procedure [2, 3], with some modifications. In a 30 L reactor, 418 g (2.5 mol) isophthalic acid, 131 g (3.3 mol) NaOH, 626 g (0.9 mol) $Al_2(SO_4)_3 \cdot 18H_2O$ and 52 g (0.6 mol) $NaAlO_2$ were dissolved in a mixture of 8.2 L H_2O/4.2 L EtOH (abs.). The mixture was refluxed for 16 h. The product was collected, washed and left to dry at RT overnight. Product mass = 470 g; Yield = 87.4 %.

1.3 Synthesis of MIL-125

MIL-125 was synthesized based on the reported procedure [4]. 15.2 g terephthalic acid (91.5 mmol) and 18.4 mL titanium isoproproxide $Ti(OiPr)_4$ (62.1 mmol) were added in a solution containing 320 mL DMF, 80 mL MeOH and 1 mL H_2O and refluxed for 72 h. At the end of the reaction, a white precipitate was recovered by filtration, washed with DMF (1.8 L) for 16 h and MeOH (1.5 L) for another 16 h. The purified product was finally recovered via filtration and activated at 200°C for 16 h, under vacuum.

1.4 Syntheis of UiO-66

UiO-66 was synthesized based on the reported procedure [4]. 3.1 g dimethyl terephthalate (16 mmol) and 3.7 g $ZrCl_4$ (16 mmol) were added in a solution containing 16 mL propan-2-ol and 5.3 mL HCl and refluxed for 70 h. At the end of the reaction, the mixture was cooled down to RT and the white solid was recovered by filtration. The powder was washed twice with EtOH ethanol at 50 °C (1g in 50 mL).

1.5 Synthesis of MOF-303

MOF-303 was synthesized based on the reported procedure [5]. 7.5 g 3,5-pyrazoledicarboxylic acid, monohydrate (43.1 mmol) was added in a solution containing 727 mL H2O and 25 mL LiOH (2.57 M) and the mixture was heated for 30 min at 120 °C. 10.4 g $AlCl3 \cdot 6H_2O$ (43.1 mmol) were then added to the solution and the mixture was further heated at 100 °C for 15 h. At the end of the reaction, the solid wash collected by filtration and washed with H_2O. The powder was subsequently washed with MeOH for 24 h in a Soxhlet apparatus and left to dry at RT. Finally, the product was activated at 150 °C for 6 h, under vacuum.

1.6 Materials characterization

PXRD patterns were recorded on a Bruker D8 Advance diffractometer working on transmission mode and equipped with a focusing Göbel mirror producing CuKα radiation (λ = 1.5418 Å) and a LynxEye detector. Infrared spectra were collected on a Nicolet iS5 FTIR ThermoFisher spectrometer. TGA data were collected on Mettler Toledo TGA/DSC 2, STAR System apparatus.

Nitrogen sorption measurements were performed at 77 K on a Micromeritics Tristar instrument.

Al-Fum was characterized by various techniques to ensure the purity of the product (Fig 1-1). As indicated from the X-ray powder diffraction (PXRD), the collected Bragg diffraction peaks of the product matched those of the calculated pattern, confirming the formation of the Al-Fum crystal structure. FT-IR analysis further indicated the coordination of aluminium atoms to the carboxylate groups of the ligand by the appearance of an asymmetric $\nu(C\text{-}O)_{as}$ and a symmetric $\nu(C\text{-}O)_{s}$ stretching modes around 1600 and 1400 cm^{-1}, respectively. A very small stretching band at 1700 cm^{-1}, which corresponds to the *ν*(C=O) vibration suggested the presence of traces of unreacted fumaric acid in the final product. The thermogravimetric analysis (TGA) of Al-Fum was conducted between RT and 600 ^{o}C and showed two major weight losses; one at $T \leq 100\ ^{o}C$ due to the removal of adsorbed solvent molecules (H_2O and EtOH) and a second one at $T = 435\ ^{o}C$, corresponding to the degradation of the organic part and the collapse of the structure, leaving oxide/hydroxide residues. The measured weight losses are similar to the calculated ones, in agreement with the chemical structure of Al-Fum ($Al(OH)(C_4O_4H_2)\cdot xH_2O$ (x~4)), although the slightly higher amount of residues suggests the presence of extra oxides/hydroxides in the product. Finally, conducting N_2 sorption measurement (77 K), Al-Fum displayed a type I isotherm, characteristic of microporous materials (Ø < 20 Å) and a calculated specific surface are of 1000 m^2g^{-1}, in agreement with the BASF product.

Supplementary Note 2: Numeric models and thermal battery optimization

2.1 General presentation of the model

A transient model has been developed to include the PV thermal battery under the laboratory test conditions. The RC circuit is clarified in Figure S17 and MATLAB is used to develop the code.

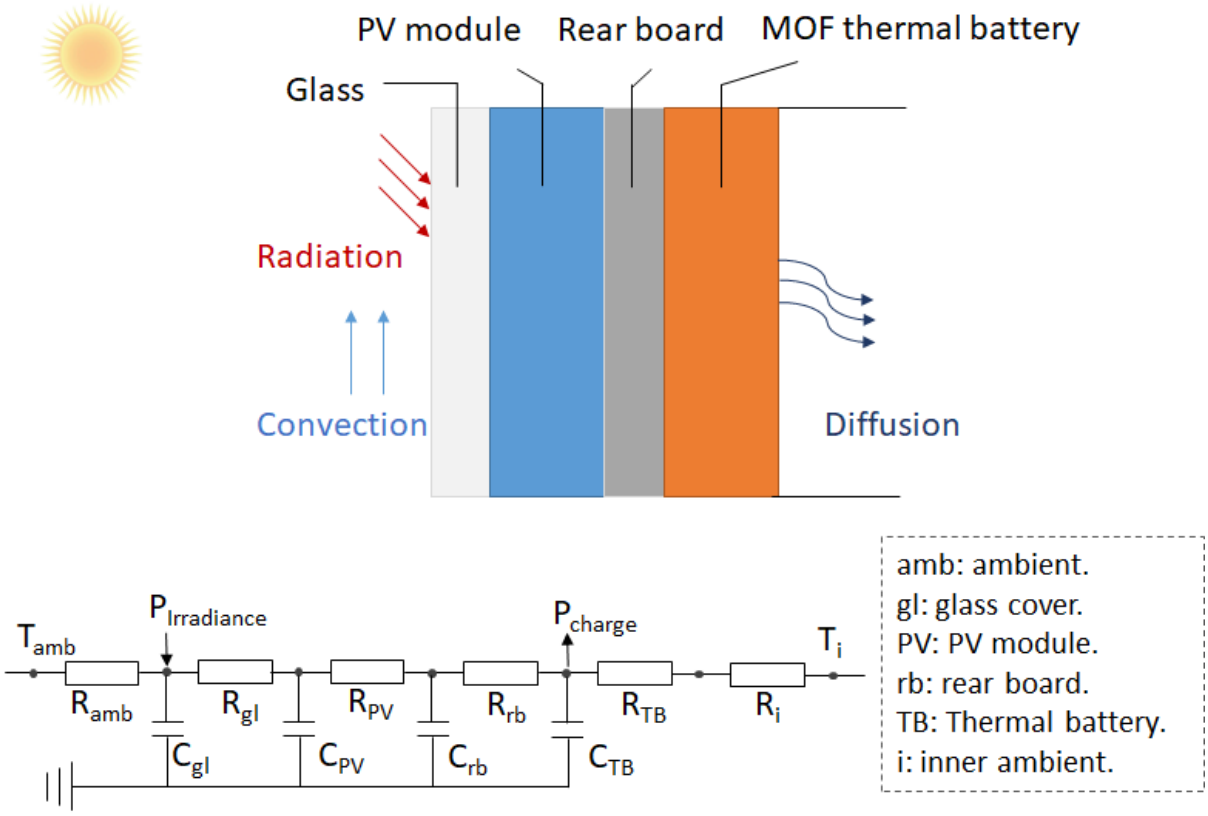

Figure S17. Simplified PVTB architecture for numeric simulation of the laboratory test and equivalent RC model.

In the experiment, the thermal battery was buckled on a larger plate surface interfaced with the solar simulator, the wind effect on the rear side was thus not taken into account in the calculation. Thermal resistances are written as l/k for conduction, $1/h_{conv}$ for convection in each layer, l is the layer thickness, k is the thermal conductivity and h_{conv} is convective coefficient, and radiative $(T_{surf}-T_{amb})/\sigma\varepsilon A\,(T_{surf}^4-T_{amb}^4)$. As the thin cavity between the supporting surface and the shield of solar simulator create a laminar flow, we calculate the convective coefficient using correlation: $h_{conv}=5.62+3.9v$, where v is the surface flow speed [6]. Inside the rear side frame, we estimate a natural convective coefficient using

correlation: $h_{conv}=1.52(T_{MOF}-T_{amb})^{1/3}$, Parameters used for the simulation are listed in Table S1.

Table S1. Key parameters and physical values of PV used for the numeric simulation

Parameter	Unit	Al-Fum
Thermal conductivity of glass cover k_{gl}	W m^{-1} K^{-1}	1
Thermal conductivity of PV module k_{PV}	W m^{-1} K^{-1}	150
Thermal conductivity of real board k_{rb}	W m^{-1} K^{-1}	150
Transmittance of glass cover τ_{gl}	-	0.9
Transmittance of PV module τ_{PV}	-	0.1
Emittance glass ε	-	0.92
Absorptivity of glass cover α_{PV}	-	0.05
Absorptivity of PV module α_{PV}	-	0.8

The thickness of each layer l_{gl}, l_{PV}, l_{rg} are 3, 0.3, 0.5 mm, respectively.

We can calculate the potential of passive cooling from convection and radiative effects. Assuming the light-heat conversion ratio is 80%, neglecting the items of C_{TB}, R_{TB}, and P_{charge} in the models. If the ambient conditions are 30°C, 50%RH (13g/kg_a) for summer, and 10°C, 80%RH (6g/kg_a) for winter, the temperature profiles are presented in Figure S11. This shows the engineering limit of passive cooling solutions of convection and radiation. Even in the situation of weak radiation and strong wind, a temperature lift of 20°C is very common. It corresponds to an efficiency loss up to 10% and much more electricity generation loss at higher radiance. The relative humidity on the surface has dropped below 15% in summer and 20% in winter in these situations where the passive cooling effects are strong and the MOF thermal battery with Al-Fum has already been charged. The cooling effects from convection and radiation are not mutually exclusive to that of MOF thermal battery.

2.2 Mass and heat conservation of the MOF thermal battery layer

A dynamic model based on energy and mass conservation is established to describe and predict the sorption performance of the thermal battery. Considering the vapor transport mechanism within MOF layer is similar to other porous materials from a macroscopic perspective, the mass transfer can be attributed to intercrystalline and intracrystalline diffusion.

$$\frac{\partial C}{\partial t} = \nabla \cdot (\mathrm{D}\nabla \mathrm{C}) - \frac{1-\varepsilon}{\varepsilon}\frac{\rho_{ad}}{M_{vap}}\frac{\partial w}{\partial t} \tag{S1}$$

$$\rho_{ad} c_p \frac{\partial T}{\partial t} = \nabla \cdot (\mathrm{k}\nabla \mathrm{T}) + (1-\varepsilon)\rho_{ad} H_{ad} \frac{\partial w}{\partial t} \tag{S2}$$

C, D, ε, M_{vap}, $\partial w/\partial t$, $\rho_{ad}c_p$, k, and H_{ad} are vapor concentration (mol·m^{-3}), diffusion coefficient in the MOF layer (intercrystalline, m^2·s^{-1}), porosity (-), molecule weight of water, and the average instantaneous rate of adsorption, the heat capacity (J·m^{-3}·K^{-1}), thermal conductivity (W·m^{-1}·K^{-1}), and enthalpy of adsorption (J·mol^{-1}), respectively. The porosity is a constant value measured by $\varepsilon=1-\rho_{ad}/\rho_{cry}$, which represent the void part within the adsorbent layer. In the laboratory condition, the advection item can be neglected since vapor pressure gradient is the main factor of the transport. For reason of simplification, we resolved the conservation equations in 1-D form for space discretization.

$$\frac{\partial C}{\partial t} = \frac{\partial}{\partial z} \cdot \mathrm{D} \frac{\partial C}{\partial z} - \frac{1-\varepsilon}{\varepsilon} \frac{\rho_{ad}}{M_{vap}} \frac{\partial w}{\partial t} \tag{S3}$$

$$\rho_{ad} c_p \frac{\partial T}{\partial t} = \frac{\partial}{\partial z} \cdot \mathrm{k} \frac{\partial T}{\partial z} + (1-\varepsilon)\rho_{ad} H_{ad} \frac{\partial w}{\partial t} \tag{S4}$$

According to the ideal gas relation, the vapor concentration can be deduced from $p=CRT$, where *p, R, T* is the pressure (Pa), universal gas constant (J·mol^{-1}·K^{-1}), and average temperature (K) of the adsorbent.

The coefficient of intercrystalline diffusion is composed of self-diffusion of vapor in air and the Knudson diffusion [7. 8]. Since the system works for coating sample, the mixture diffusion is neglected. The size of Aluminium Fumarate crystal is around 900 nm, characterized with scanning electron microscopy. The Knudsen diffusivity is at the level of 10^{-5} m^2· s^{-1}, estimated from $D=d/3(8RT/\pi M_{vap})^{0.5}$, where *d* is characteristic void size of the crystal [9, 10]. For simplification we assume the Al-Fum crystals are under closest packing [11].

The heat capacity and thermal conductivity terms should incorporate the dry MOFs and the adsorbed vapor, which can be treated as the liquid. The measurement used a μSC and TCi sensor [12]. Parameters used for the simulation are listed in Table S2 [13-15].

Table S2. Key parameters and physical values of MOF layer used for the numeric simulation

parameter	Unit	Al-Fum
Intercristalline vapor diffusion coefficient D	m^{2}s^{-1}	1.2x10^{-5}
heat capacity c_p	J g^{-1} K^{-1}	1.2
thermal conductivity *K*	W m^{-1} K^{-1}	0.12
thermal conductivity *K coated on support*	W m^{-1} K^{-1}	3
enthalpy of adsorption H_{ad}	kJ mol^{-1}	50.8
universal gas constant *R*	J mol^{-1} K^{-1}	8.314
Porosity ε	-	0.475
Crystal radius r_{cry}	nm	900
Intracristalline vapor diffusion coefficient D_μ	m^2 s^{-1}	5 x10^{-12}

In Eq (S3) and (S4), the term *w* is the water uptake within the adsorbent, and the average instantaneous rate of adsorption, *∂w/∂t* is approximated with the linear driving force model (LDF) [16, 17].

$$\frac{\partial \mathrm{w}}{\partial \mathrm{t}} = k_L(w_{eq} - w) = \frac{15D_\mu}{r_{cry}^2}(w_{eq} - w) \tag{S5}$$

Where w_{eq} is the equilibrium vapor concentration in the function of local temperature *T* and vapor pressure *P*, which can be fitted by a dual-site Langmuir method [18].

$$w_{eq}(p,T) = w_b(1 - wt(p,T)) + w_a(p,T)wt(p,T)$$

$$w_b(p,T) = w_{b,\infty}\frac{b_b p}{1 + b_b p}$$

$$w_a(p,T) = w_{a,\infty}\frac{b_a p}{1 + b_a p} + b_c p$$

$$\mathrm{b}_i = \mathrm{b}_{i,\infty}\exp\left(\frac{E_i}{RT}\right), i = a, b, c$$

$$wt(p,T) = \left(\frac{\exp\left(\frac{\ln(p) - \ln(p_{step}(T))}{\sigma(T)}\right)}{1 + \exp\left(\frac{\ln(p) - \ln(p_{step}(T))}{\sigma(T)}\right)}\right)^{\gamma} \tag{S6}$$

$$\sigma(T) = \chi_1 \exp\left(\chi_2\left(\frac{1}{T_0} - \frac{1}{T}\right)\right)$$

$$p_{step}(T) = p_{step,0}\exp\left(\frac{-H_{step}}{R}\left(\frac{1}{T_0} - \frac{1}{T}\right)\right)$$

The water uptake at a certain pressure and temperature $w_{eq}(p, T)$ is calculated from two Langmuir-terms (w_b and w_a), representing the adsorption before and after the step in the uptake. *wt(p, T)* is a weighting function that depends on the pressure *p*, the temperature *T* and the pressure p_{step} at which the uptake step occurs. Further symbols w_∞, b_i, E_i, and χ_1, χ_2 represent fit parameters.

The van't Hoff relation is used to develop the isosteric adsorption heat.

$$\frac{H_{ad}(w,T)}{RT^2} = -\frac{\partial(lnP)}{\partial(T)} \quad \text{(S7)}$$

The fitting parameters of Al-Fum isotherms are shown in Table S3. The fitting results are shown in Figure S4.

Table S3. Key parameters of aluminium fumarate for the isotherm calculation

parameters	**Unit**	**Al-Fum**
$p_{step,0}$	Pa	2080
H_{Step}	kJ mol^{-1}	-50.8
$w_{a,\infty}$	g g^{-1}	0.087
$b_{a,\infty}$	Pa^{-1}	2.1 x10^{-12}
E_a	kJ mol^{-1}	50.5
$W_{b,\infty}$	g g^{-1}	0.402
$b_{b,\infty}$	Pa^{-1}	7.0 x10^{-13}
E_b	kJ mol^{-1}	55.5
$b_{c,\infty}$	Pa^{-1}	6.8 x10^{-12}
E_c	kJ mol^{-1}	36.4
χ_1	K^{-1}	0.065
χ_2	-	-1100
γ	-	1.7
T_0	K	313.15

2.3 PV generation model

The open-source pvlib python tool box is used to simulate power generation of PV systems in different cities under different scenarios [19]. As the input data for the simulation, clear-sky irradiance is extracted for each given location from the McClear dataset, considering both accuracy and accessibility [20].

Given the computed cell temperature T_m and global in-plane irradiance E, DC (P_{dc}) and AC power output (P_{ac}) is calculated using PVWatts module model and inverter model (Eq.S8 to S10). As shown in Table S4, the numerical assumptions for PV system characteristics are generally taken from the default settings of PVWatts model [21].

$$P_{dc} = \frac{E}{1000} \cdot P_{dc0} \cdot [1 + \gamma \cdot (T_m - 25)] \cdot (1 - \eta_{system}) \quad \text{(S8)}$$

$$\eta = \frac{\eta_{nom}}{\eta_{ref}} (-0.0162 \frac{P_{dc}}{P_{dc0}} - 0.0059 \frac{P_{dc0}}{P_{dc}} + 0.9858) \quad \text{(S9)}$$

$$P_{ac} = \min(\eta P_{dc}, P_{ac0}) \quad \text{(S10)}$$

where: P_{dc0} is DC power at Standard Reporting Conditions (SRC), W; P_{ac0} is AC nameplate rating of PV system, W; γ is temperature coefficient, °C^{-1}; η_{system} is DC power losses; η_{nom} is nominal inverter efficiency; η_{ref} is reference inverter efficiency.

Table S4. Characteristics of PV systems in the power generation model

Parameters	**Unit**	Value
Module construction	-	Glass/glass
Mounting type	-	Close roof
Module tilt	°	30
Module azimuth	°	180 (equator orientated)
DC power losses	-	0.14
Temperature coefficient	1/°C	-0.0035
Nominal inverter efficiency	-	0.96
Reference inverter efficiency	-	0.9637

2.4 Model validation

We compare the simulated charging and discharging performance with experimental results in laboratory conditions to validate the heat and mass transfer model. In the discharging process, the item of $P_{irradiance}$ doesn't exist and P_{charge} is replaced by $P_{discharge}$ with equal quantity in total but inversed direction.

The discharging was performed in a DVS with a coating samples. The temperature maintained at 25°C with variable humidity. The charging was performed under the solar simulator with 1 sun condition. The room maintained at 25°C, ~40%. The convection mode was tuned with one strong wind around 2 m/s to imitate forced ventilation (FV). Both the small and up-scale samples were measured and compared. Results are presented in Figure S18&S19.

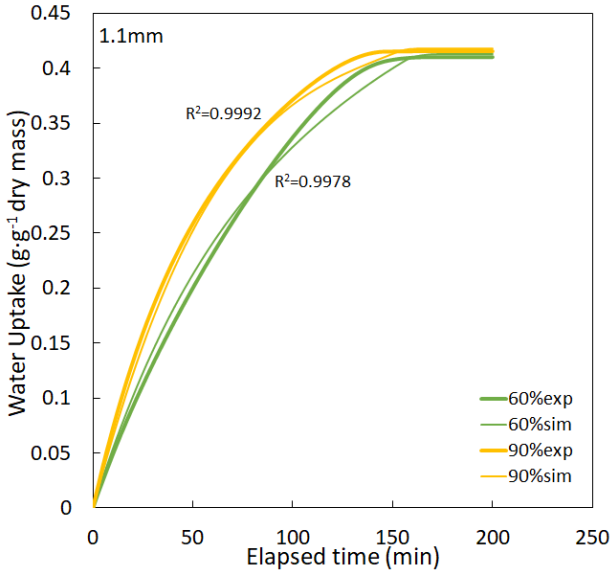

Figure S18. Discharging process under constant conditions with measured and simulated water uptake in function of time.

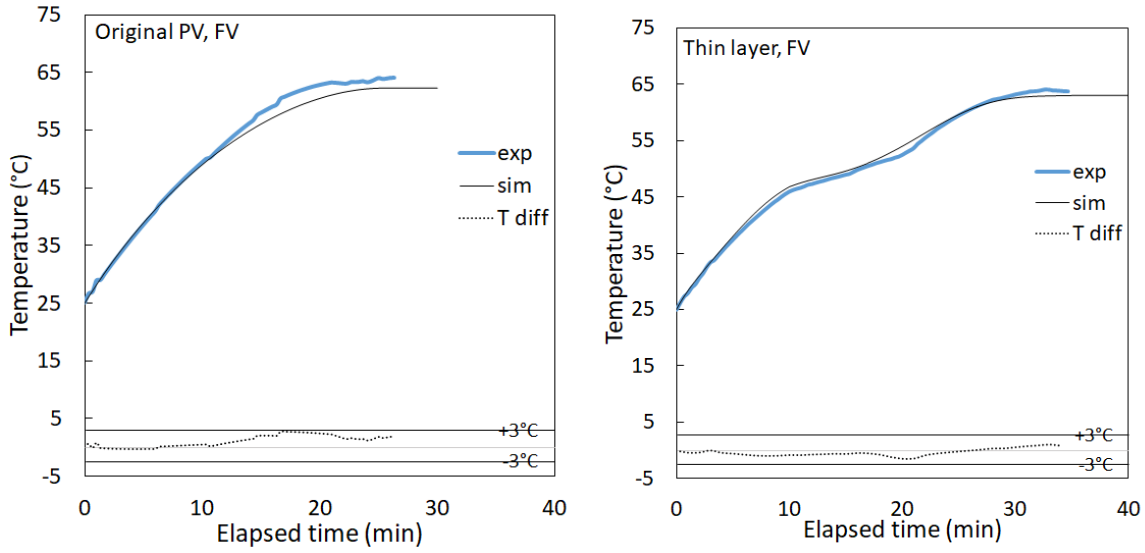

Figure S19. Charging process under constant conditions with measured and simulated PV temperature in function of time.

2.5 Optimization of the design

We studied the practicability, adaptability and robustness of the thermal battery according to several metrics in charging process. We defined temperature plateau and effective time as the average temperature of the PV and duration when the charging process produces a cooling effect, and T lift as the temperature elevation of the PV due to additional thermal resistance (Figure S20).

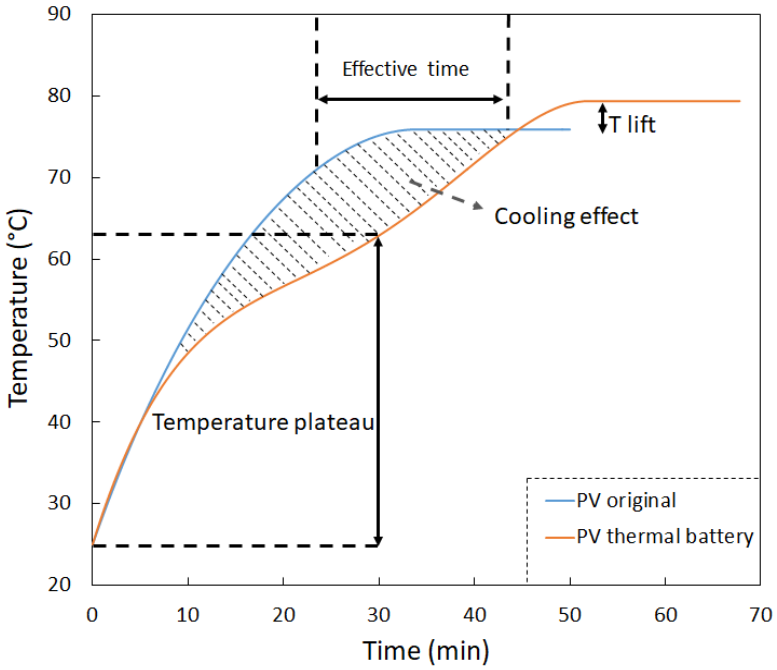

Figure S20. Metrics to evaluate charging performance of MOF thermal battery. Shaded zone represents charging capacity, determined by the water uptake and mass deployed. Temperature plateau is determined by the position of inflection point and mass deployed. Effective time is determined by the water uptake and mass deployed. The additional resistances of coating layers result in a temperature lift which exists in the entire charging process and deviates the temperature plateau from desorption temperature predicted with sorption isotherms (the thermodynamic limits).

We ran a parametric study based on the coating layer thickness, air conditions, and the irradiance. For the reason of simplification, we calculated only wind speed larger than 1m/s in neglecting the buoyancy effects in natural ventilation.

The simulated charging performance of an Al-Fum thermal batter is shown in Figure S21. Whether the charging process of the thermal battery can have cooling effect depends on a series of variables. The effective working range is between the black dash lines and the red lines. A thermal battery should be thick enough to enable the intra-day operation but not too thick that temperature lift offsetting the cooling effect.

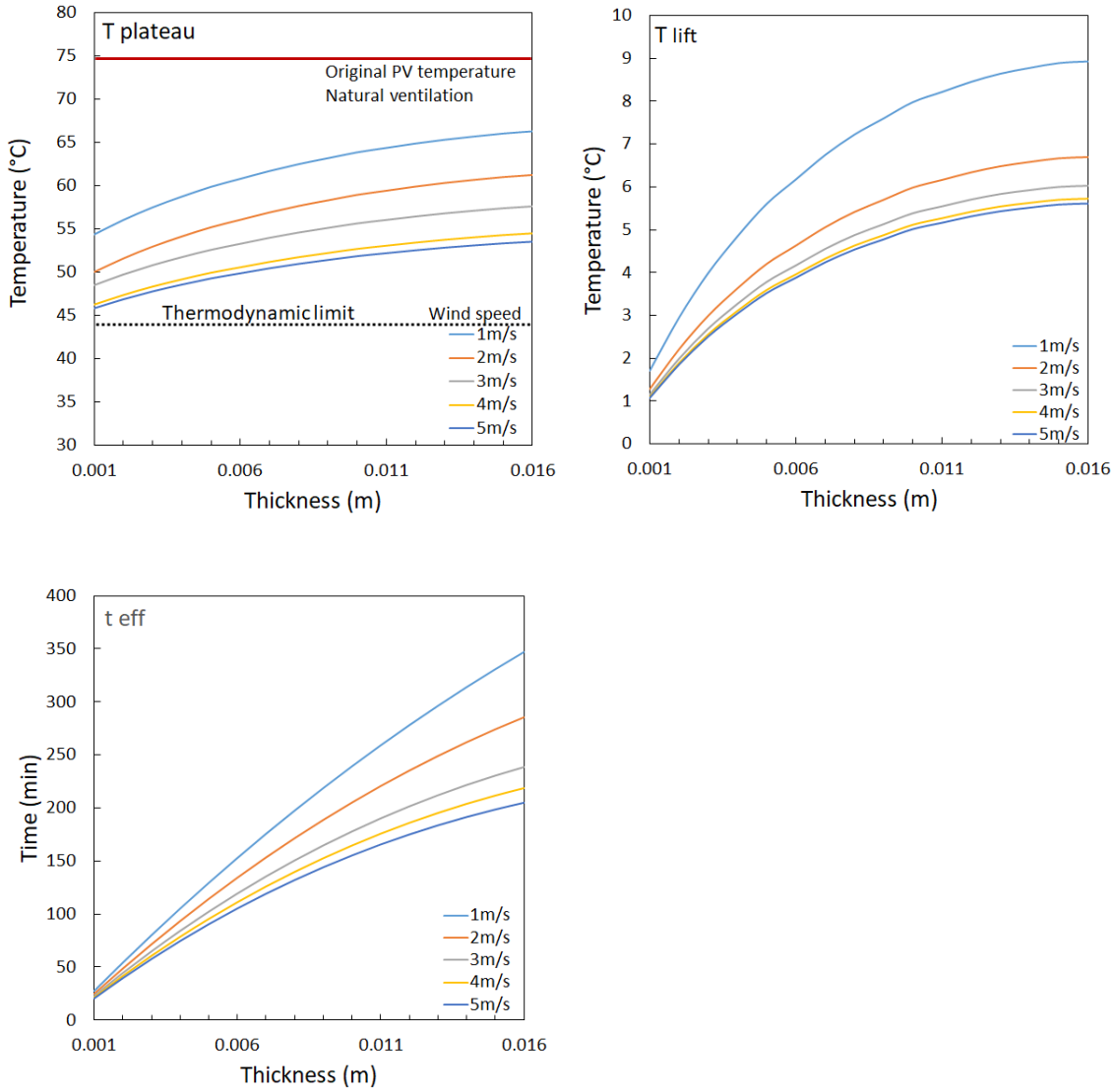

Figure S21. Charging performance of Al-Fum thermal battery with various layer thickness. a, Temperature plateau, **b,** Temperature rise at the end, **c**, Effective cooling time in summer of the temperate climate with 30°C, 50%RH, 1000W/m^2, various wind speeds. The red line is the original PV temperature under natural ventilation mode (<1m/s). A T plateau beyond it will not create cooling effect to compensate the adverse effect of the additional thermal resistance. The black dash line is the minimum temperature required by Al-Fum at these conditions to desorb water.

As the T-lift and effective time is to some extent proportional to the thickness, we focus on the analysis of temperature plateau in estimating the efficiency of the thermal battery.

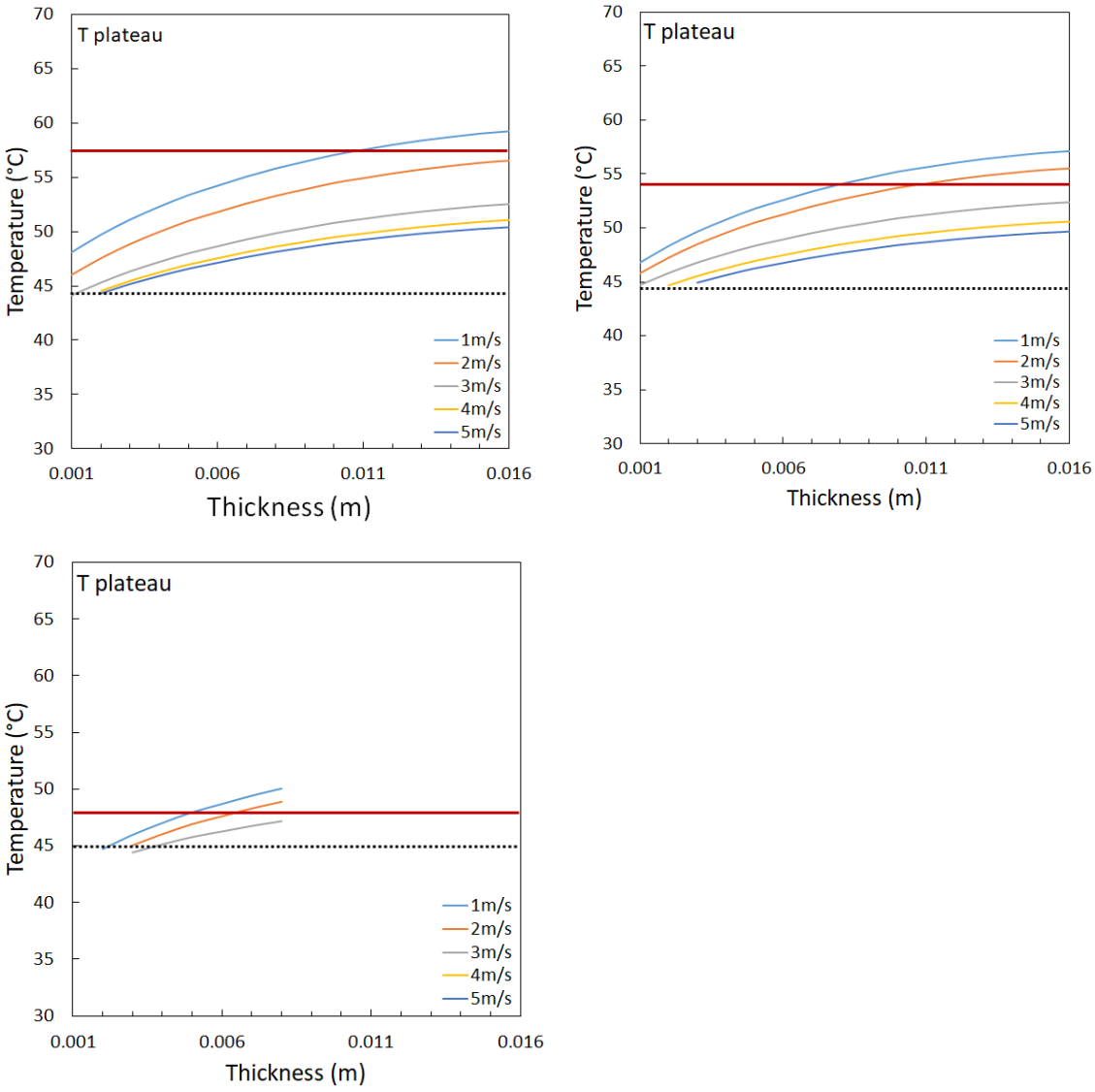

Figure S22. Influence of solar irradiance on the temperature plateau of Al-Fum thermal battery with various layer thickness. a, 800W/m^2, **b,** 600W/m^2, **c,** 400W/m^2 in 30°C, 50%RH, various wind speeds.

As shown in Figure S22 with various radiance level, the configuration of the thermal battery must be carefully engineered so that it can have a positive effect on the electricity generation. The temperature of the PV can drop with less intensive irradiance, which narrows the operation range of the thermal battery. When the solar radiance is as weak as 400W/m^2 the charging can merely produce effective cooling. However, the electricity generation at higher irradiance is more important to the general performance in reality. The ventilation is also positive for cooling the PV not only because of the higher convective thermal transfer but also the facilitated desorption.

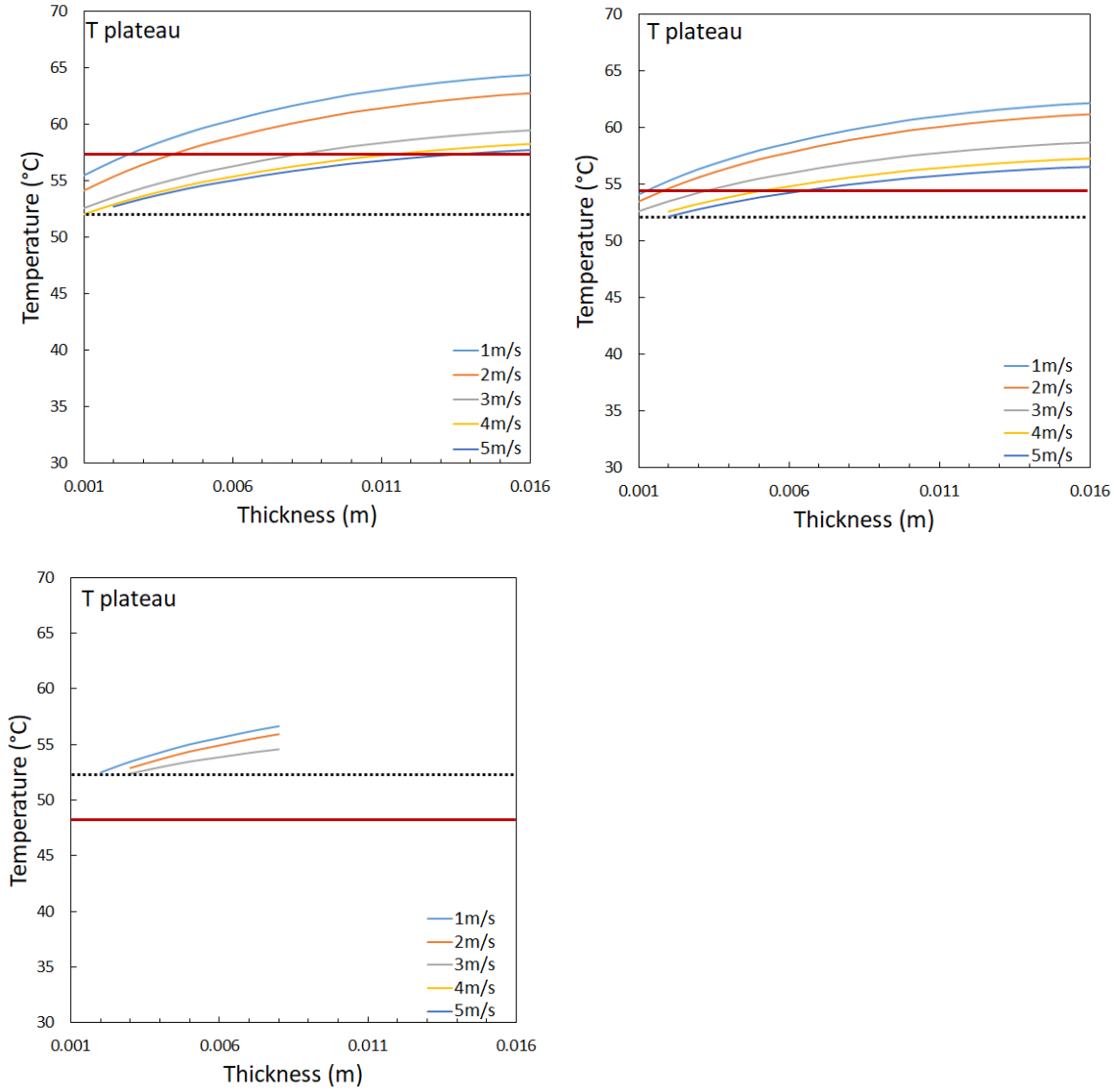

Figure S23. Influence of solar irradiance on the temperature plateau of MIL-160(Al) thermal battery with various layer thickness. a, 800W/m^2, **b,** 600W/m^2, **c,** 400W/m^2 in 30°C, 50%RH, various wind speeds.

As shown in Figure S23 with various radiance level, the operation range of MIL-160(Al) is much smaller than Al-Fum. The system is less tolerant to the thickness of thermal battery since the elevated temperature plateau can more easily surpass the original temperature. When the solar radiance is as weak as 400W/m^2 the red line is below the broken line, which means there is no cooling effect produced at all.

Supplementary Note 3: Climate adaptability of the MOFs

The weather conditions can largely move the thermodynamic limits of the thermal battery thus narrow or broaden the operation range. The temperature plateau of the Al-Fum thermal battery in various weather conditions is shown in Figure S24. In general, it is more difficult to charge the thermal battery in a more humid weather, while the discharging process is more valuable due to the dehumidification needs. Charging in winter is more difficult due to the coupled effects that kinetics are slower and irradiance is lower.

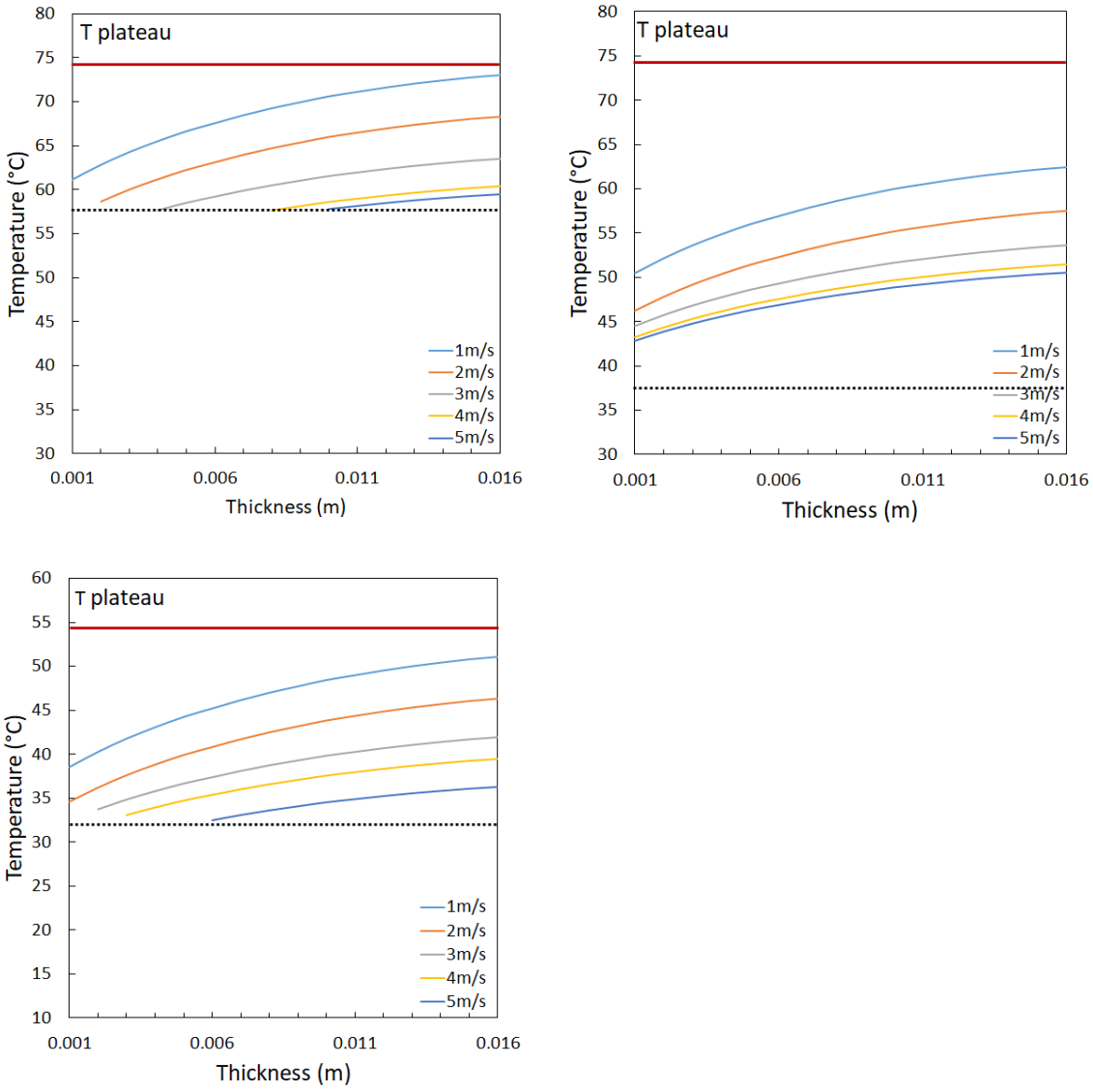

Figure S24. Influence of climate conditions on the temperature plateau of Al-Fum thermal battery with various layer thickness. a, Humid summer, 30°C, 50%RH, 1000W/m^2, **b,** Dry summer, 30°C, 30%RH, 1000W/m^2 **c,** Winter, 10°C, 80%RH, 1000W/m^2, various wind speeds.

We consider 5 MOFs with different hydrophilic character and normalize their water uptake to focus on the thermodynamics factors for their climate adaptability (Figure S25). MIL-101(Cr) and PIZOF-2(Zr) are two benchmark materials even less hydrophilic than Al-Fum [22, 23].

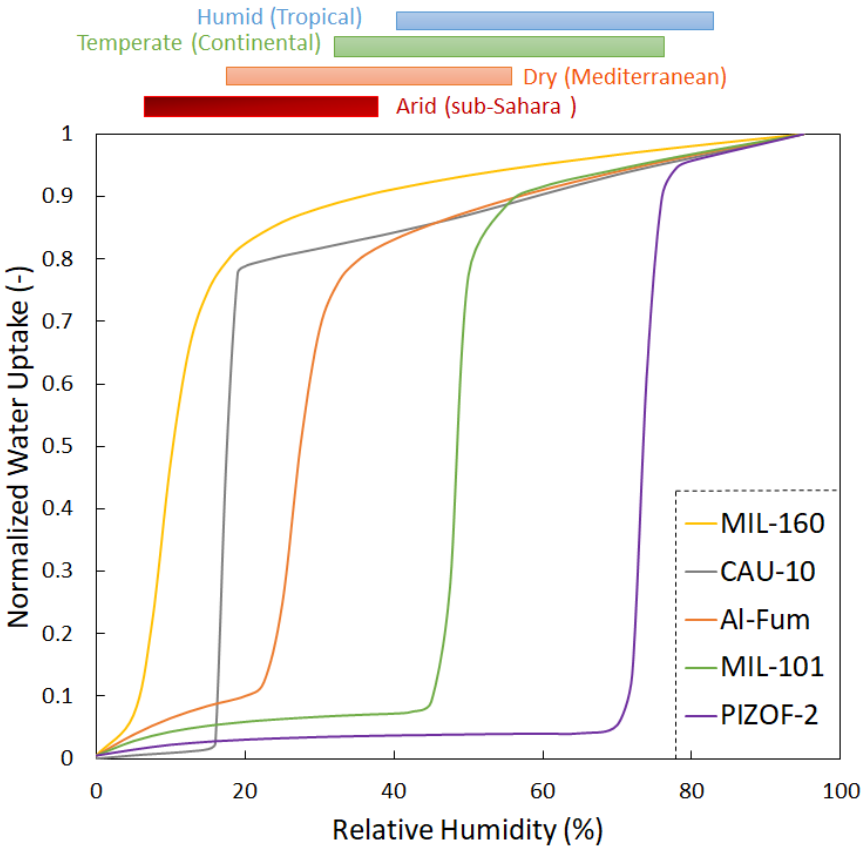

Figure S25. MOFs with different hydrophilic character and their adaptability to climates. The preferred working ranges of relative humidity are marked with colored legends above.

We explore the discharging and charging capacity of these MOFs in European climates in Figure S26 and S27. MOFs with inflection points on the right of 50%RH will be difficult to be charged in relatively dry weather. Although their charging time window lasts longer than more hydrophilic MOFs, their cyclic water uptake, thereby the energy-economic benefits on unit mass, is low.

Two MOFs with similar energy storage but different inflection points also differentiate from each other significantly, such as MIL-160 and Al-Fum. MIL-160 has a smaller charging time window, cools the PV at a higher temperature. Therefore, we can observe a cooling effect more intensive than Al-Fum for unit mass deployed. Yet, its total cooling effect and effective time is much less in most cases due to its higher temperature plateau.

The charging/discharging performance of a MOF is better in drier weather, and therefore, the incremental electricity generation is higher. However, the added value of a thermal battery in drier weather is not necessarily high because of less needs in dehumidification. The design strategy of the BIPV-thermal battery needs additional adaptation to different

climates. For instance, in most regions of Europe, the dehumidification needs occur more frequently in winter. Especially for Mediterranean city like Athens, to avoid increasing on sensible heat loads, the air used for the discharging process should come from outdoor or adjacent zones instead of indoor space and not be conducted to the indoor environment. The corresponding benefits on dehumidification is then lost.

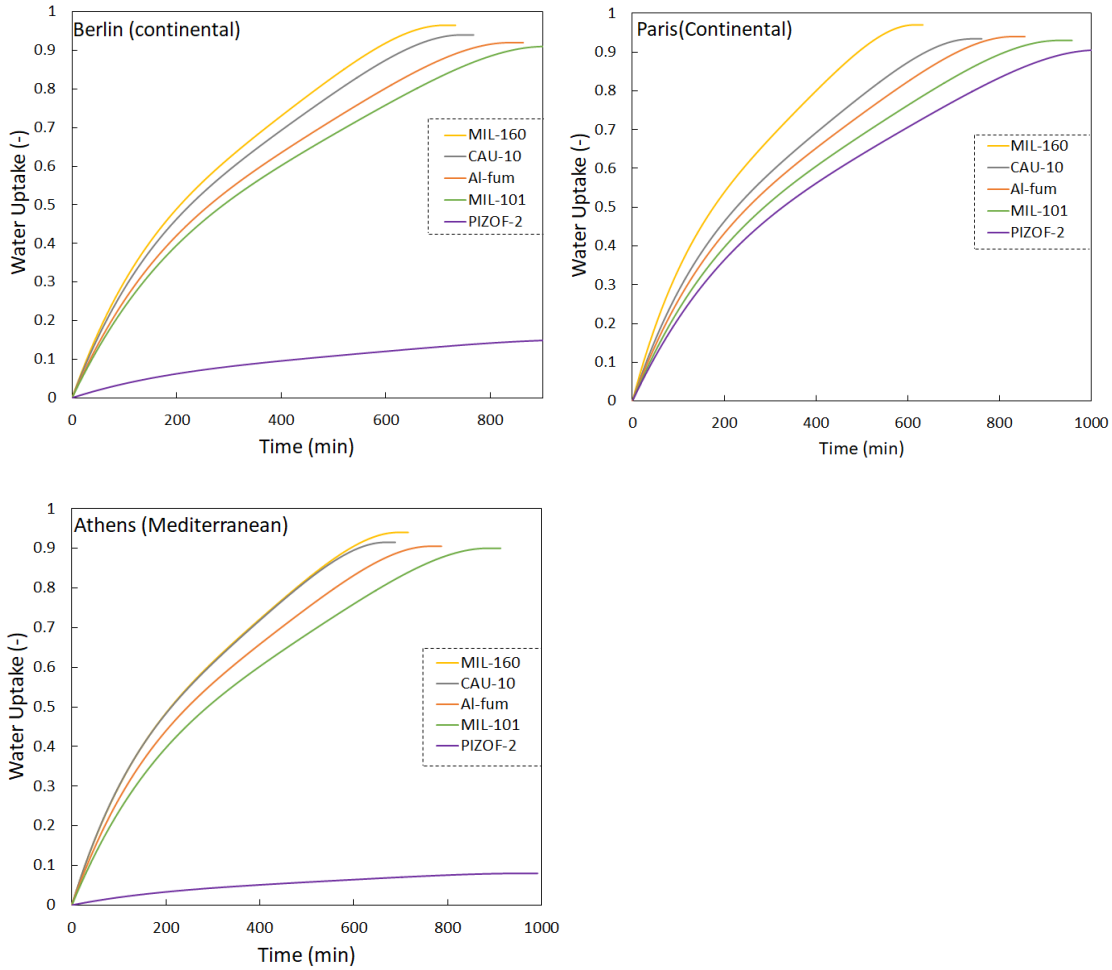

Figure S26. Discharging capacity of the MOFs in a summer day in Berlin (Continental), Paris (Continental) and Athens (Mediterranean).

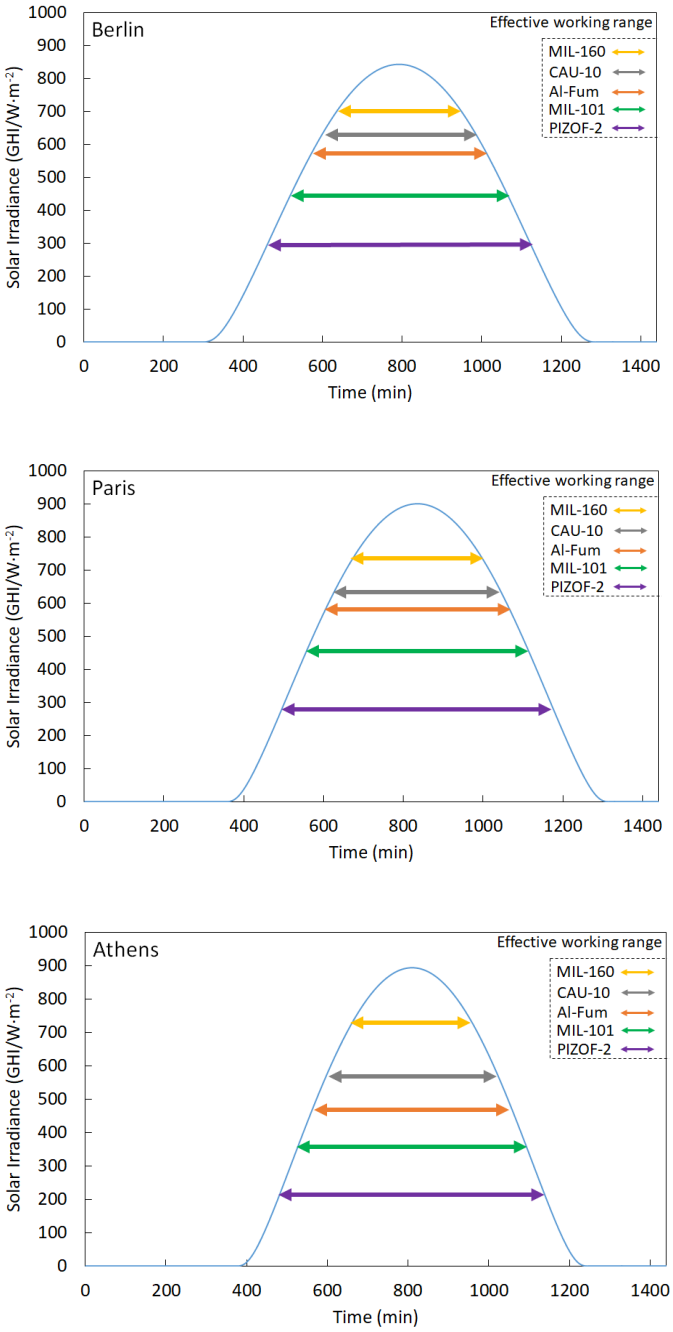

Figure S27. Charging effective time window of the MOFs in a summer day in Berlin (Continental), Paris (Continental) and Athens (Mediterranean).

Supplementary Note 4: Economic Analysis model

LCOE is calculated as the net present value of the electricity cost over the lifetime of the PV system

$$\mathrm{LCOE} = \frac{\sum_{t=0}^{N} \frac{I(t) + OM(t)}{(1+r)^t}}{\sum_{t=0}^{N} \frac{E(t)}{(1+r)^t}} \tag{S11}$$

Where *I* is the annual investment of the system in the region, *OM* are annual operation and maintenance expenses, E_t is electricity generation in the year *t*, *N* is the financial lifetime in years, *r* is the nominal discount rate.

We can calculate the LCOE of an original PV ($LCOE_{PV}$) and PV thermal battery ($LCOE_{PVTB}$). The investment is an aggregation of manufacturing cost, including module, inverter and labour costs, plus associated components and capital expenditure, and we assume the fixed cost is not scaled with the power. $I=C_m+C_{fix}$. Since the form of MOF thermal battery has no distinction to a submodule of the PV, its installation is a one-time operation no matter on a new or existing system, and there is no consumable component in functioning, it is not imprudent to calculate the investment of the thermal battery as a part of the manufacturing cost, scaled with the power and independent from the fixed cost. By equalizing the LCOE of original PV and PV thermal battery, $LCOE_{PV}=LCOE_{PVTB}$, we obtained the iso-cost relation for installing the thermal battery, which gives the maximum allowable cost of the thermal battery for the investment to be economically viable.

$$\frac{C_{m.PV} + C_{fix} + \sum_{t=0}^{N} \frac{OM_{PV}}{(1+r)^t}}{\sum_{t=0}^{N} \frac{E_{PV}}{(1+r)^t}} = \frac{C_{m.PV} + C_{m.TB} + C_{fix} + \sum_{t=0}^{N} \frac{OM_{PV} + OM_{TB}}{(1+r)^t}}{\sum_{t=0}^{N} \frac{E_{PVTB}}{(1+r)^t}} \tag{S12}$$

The *OM* is simplified as proportional to the manufacturing cost $OM=k\cdot C_m$. Energy yield of the PV integrated with thermal battery is assumed as an averaged constant improvement to the original PV, $E_{PVTB}=(1+\delta)\cdot E_{PV}$, and degraded with a same rate to the original module $E(t)=E_0\cdot(1-deg)^t$, where E_0 is energy generation in the first year. After trivial transformation of *eq (S12)*, we can obtain an analytical solution to the $C_{m,TB}$:

$$C_{m.TB} = C_{m.PV} \cdot \delta + \frac{C_{fix} \cdot \delta}{1 + \sum_{t=0}^{N} \frac{k}{(1+r)^t}} \tag{S13}$$

The obtained $C_{m,TB}$ is the upper limit cost of an isolated PV thermal battery system, such as in the scenario of utility PV. Assuming $C_{m,TB}$ is determined solely by the mass of the MOF deployed , we can then have the maximum allowable unit cost of the MOF:

$$C_{MOF} = \frac{C_{m,TB}}{m_{MOF}} \tag{S14}$$

Note that C_{MOF} here is an agglomerated cost on unit MOF mass.

However, in the BIPV scenario presented in this paper, we can further estimate the integration benefits on system level. We calculate the equivalent energy to remove the same volume of moisture in a discharging-charging cycle if dehumidification is realized by a

compressor-based air-conditioner. The total gain in electricity due to passive dehumidification can be calculated by:

$$\mathrm{E}_{add} = \frac{m_{MOF} \cdot \mathrm{WU} \cdot H_{ad}}{\eta \cdot COP_{ac}} \quad \text{(S15)}$$

Where *WU* is the cyclic water uptake of MOF, η is the conversion efficiency of the PV panel and COP_{ac} is the electricity-to-heat efficiency of the air-conditioner, taken as 3. Furthermore, we assume that the electricity used to power the air-conditioner is all from the PV generation. Then *eq (S12)* becomes

$$\frac{C_{m.PV} + C_{fix} + \sum_{t=0}^{N} \frac{OM_{PV}}{(1+r)^t}}{\sum_{t=0}^{N} \frac{E_{PV}}{(1+r)^t}} = \frac{C_{m.PV} + C_{m.TB} + C_{fix} + \sum_{t=0}^{N} \frac{OM_{PV+}OM_{TB}}{(1+r)^t}}{\sum_{t=0}^{N} \frac{E_{PVTB} + E_{add}}{(1+r)^t}} \quad \text{(S16)}$$

And the new maximum allowable unit price of $C_{MOF\text{-}n}$ can be obtained by resolving this equation. In fact, we can find a mathematical relation between the electricity generation improvement rate δ and the conversion efficiency η since the electricity generated is compounded from the solar conversion efficiency and several other factors. However, this requires an optimal design of the system and long-term data requisition in experiments to be precise, which is beyond the scope of this paper. For the reason of a first-order estimation, we neglected these physics details and calculated the C_{MOF} based on the field test results.

Parameters used for the economic analysis are listed in Table S5. The sensibility of the maximum allowable cost of the thermal battery to several financial metrics are shown in Table S6.

Table S5. Key parameters of PV system for the LCOE calculation [24, 25].

parameters	**Unit**	**2019**	**2030**
Solar efficiency η	%	18.9	24
Surface coverage ratio	%	65	65
Surface power density	$W_p\,m^{-2}$	123.2	123.2
Manufacturing cost *CmPV*	€ W_p^{-1}	1.56	0.94
Manufacturing cost *CmPV*	€ m^{-2}	192.56	116
Fixed cost C_{fix}	€ W_p^{-1}	1.13	0.68
Fixed cost C_{fix}	€ m^{-2}	139.44	83.52
Operation and maintenance expenses *OM*	€ W_p^{-1} yr^{-1}	0.078	0.047
Operation and maintenance expenses *OM*	€ m^{-2} yr^{-1}	9.63	5.8
Ratio of OM to manufacturing cost *k*	-	0.05	0.05
Paris equivalent sunlight time	hour	1662	1662
Degradation rate *deg*	%	1%	1%
Deployed Al-Fum mass	kg m^{-2}	1.89 (==2.9 for 100% surface coverage ratio)	same

Table S6. LCOE and MOF cost sensibility on financial conditions.

Project Lifetime (yr)	Discount rate (%)	LCOE (ct kWh^{-1})	Allowable $Cost_{MOF}$ (€ kg^{-1})	$Cost_{mof}$ with dehumidification (€ kg^{-1})
2019 market				
25	2%	13.63	7.01	9.95
25	5%	16.5	7.29	10.36
25	8%	19.73	7.52	10.69
20	5%	17.7	7.39	10.51
30	5%	15.78	7.22	10.25
2030 market				
25	2%	6.44	4.22	5.64
25	5%	7.81	4.37	5.87
25	8%	9.31	4.5	6.06

References

[1] Permyakova, A., Skrylnyk, O., Courbon, E., Affram, M., Wang, S., Lee, U.-H., Valekar,, A. H. Nouar, F., Mouchaham, G., Devic, T., De Weireld, G. et al. Synthesis optimization, shaping, and heat reallocation evaluation of the hydrophilic Metal–organic framework MIL-160(Al). *ChemSusChem*, **10,** 1419-1426 (2017).

[2] Wahiduzzaman, M., Lenzen, D., Maurin, G., Stock, N., Wharmby, M. T. Rietveld fefinement of MIL-160 and its structural flexibility upon H_2O and N_2 adsorption. *Eur. J. Inorg. Chem.*, **32,** 3626-3632 (2018).

[3] Lenzen, D., Bendix, P., Reinsch, H., Fröhlich, D., Kummer, H., Möllers, M., Hügenell, P. P. C. R., Gläser, R., Henninger, S., Stock, N. Scalable green synthesis and full-scale test of the Metal–Organic Framework CAU-10-H for use in adsorption-driven chillers. *Adv. Mater.*, **30,** 1705869 (2018).

[4] Cui, S., Qin, M., Marandi, A., Steggles, V., Wang, S., Feng, X., Nouar, F., Serre, C. Metal-organic frameworks as advanced moisture sorbents for energy-efficient high temperature cooling. *Sci. Rep.* **8,** 15284 (2018).

[5] Hanikel, N., Prévot, M. S., Fathieh, F., Kapustin, E. A., Lyu, H., Wang, H., Diercks, N. J., Glover, T. G., Yaghi, O. M. Rapid cycling and exceptional yield in a Metal-Organic Framework water harvester. *ACS Cent. Sci.* **5,** 1699-1706 (2019).

[6] Goiaa, F., Perino, M., Haase, H. A numerical model to evaluate the thermal behaviour of PCM glazing system configurations. *Energy Build.* **54,** 141-153 (2012).

[7] Kim, H., Yang, S., Rao, S. R., Narayanan, S., Kapustin, E. A., Furukawa, H., Umans, A. S., Yaghi, O. M., Wang, E. N. Water harvesting from air with metal-organic frameworks powered by natural sunlight. *Science* **356,** 430 (2017).

[8] Ruthven, D. M., DeSisto, W. J., Higgins, S. Diffusion in a mesoporous silica membrane: Validity of the Knudsen diffusion model. *Chem. Eng. Sci.* **64,** 3201-3203 (2009).

[9] Welty, J. R., Wicks, C. E., Rorrer, G., Wilson, R. E. *Fundamentals of Momentum, Heat, and Mass Transfer*, John Wiley & Sons (2009).

[10] Cussler, E. L. *Diffusion mass transfer in fluid systems: third edition.* Cambridge University Press (2009).

[11] Alonso, M., Sainz, E., Lopez, F., Shinohara, K. Void-size probability distribution in random packings of equal-sized spheres. *Chem. Eng. Sci.* **50,** 1983-1988 (1995).

[12] Cui, S., Marandi, A., Lebourleux, G., Thimon, M., Bourdon, M., Chen, C., Severino, M. I., Steggles, V., Nouar, F., Serre C. Heat properties of a hydrophilic carboxylate-based MOF for water adsorption applications. *Appl. Therm. Eng.* **161,** 114135 (2019).

[13] Heinke, L., Tzoulaki, D., Chmelik, C., Hibbe, F., van Baten, J. M., Lim, H., Li, J., Krishna, R., Käger, J. Assessing guest diffusivities in porous hosts from transient concentration profiles. *Phys. Rev. Lett.* **102,** 065901 (2009).

[14] Jeremias, F., Fröhlich, D., Janiak, C., Henninger, S. K. Advancement of sorption-based heat transformation by a metal coating of highly-stable, hydrophilic aluminium fumarate MOF. *RSC Adv.* **4,** 24073 (2014).

[15] Splith, T., Fröhlich, D., Henninger, S. K., Stallmach, F. Development and application of an exchange model for anisotropic water diffusion in the microporous MOF aluminum fumarate. *J. Magn. Reson.* **291,** 40-46 (2018).
[16] Glueckauf, E. Theory of chromatography. Part 10.-Formulæ for diffusion into spheres and their application to chromatography. *Trans. Faraday Soc.* **51,** 1540-1551 (1955).
[17] Sircar, S., Hufton, J. Why does the linear driving force model for adsorption kinetics work? *Adsorption* **6,** 137-147 (2000).
[18] Lenzen, D., Zhao, J., Ernst, S.-J., Wahiduzzaman, M., Inge, A. K., Fröhlich, D., Xu, H., Bart, H.-J., Janiak, C., Henninger, S., Maurin, G., Zou, X., Stock, N. A metal–organic framework for efficient water based ultra-low-temperature-driven cooling. *Nat. Commun.* **10,** 3025 (2019).
[19] Holmgren, W. F., Hansen, C. W., Mikofski, A. M. Pvlib Python: a Python Package for Modeling Solar Energy Systems. *J. Open Source Softw.* **3,** 884 (2018).
[20] Yang, D., Bright, J. M. Worldwide validation of 8 satellite-derived and reanalysis solar radiation products: A preliminary evaluation and overall metrics for hourly data over 27 years. *Sol. Energy* 1–17 (2020).
[21] Dobos, A. *PVWatts Version 5 Manual.* 2014, NREL/TP-6A20-62641.
[22] Seo, Y.-K., Yoon, J. W., Lee, J. S., Hwang, Y. K., Jun, C.-H., Chang, J.-S., Wuttke, S., Bazin, P., Vimont, A., Daturi M. et al. Energy-efficient dehumidification over hierarchically porous metal–organic frameworks as advanced water adsorbents. *Adv. Mater.* **24,** 806-810 (2012).
[23] Schaate, A., Roy, P., Preusse, T., Lohmeier, S., Godt, A., Behrens, P. Porous interpenetrated zirconium-organic frameworks (PIZOFs): a chemically versatile family of metal-organic frameworks. *Chem.-Eur. J.* **17,** 9320 (2011).
[24] ICARES, *BIPV boost: Competitiveness status of BIPV solutions in Europe.* 2020, Available online version https://bipvboost.eu/public-reports/download/cost-competitiveness-status-of-bipv-solutions-in-e
[25] The SunShot Initiative's 2030 Goal (2016). 3¢ per Kilowatt Hour for Solar Electricity. https://www.energy.gov/sites/prod/files/2016/12/f34/SunShot%202030%20Fact%20Sheet-12_16.pdf